DECEMBER 2014, NO 3

Scripta-Ingenia

O segredo da raiz de dois

Pitágoras, pormenor de Scuola di Atene*, Raphael, 1509*

Já por volta do ano 550 a.C. Pitágoras ensinava aos seus discípulos que se a, b e c são as medidas dos lados de um triângulo rectângulo, então a equação

$$a^2 + b^2 = c^2$$

verifica-se sempre que a e b são os catetos do triângulo rectângulo e c é a sua hipotenusa.
Nessa altura o conhecimento não era livre e acessível ou muito menos universal. Era, ao invés, um privilégio de uma classe muito reduzida de indivíduos os quais tinham de dar provas do seu total empenho e interesse para poderem integrar essa classe tão especial e privilegiada e terem assim acesso ao conhecimento.
A Filosofia Pitagórica assentava na ideia de que os números são perfeitos e que para além dos números inteiros existiam apenas os racionais que podiam ser obtidos por construções geométricas.
As suas investigações, porém, levaram-nos à descoberta de uma verdadeira bomba destruidora da sua filosofia. Descobriram que o número $\sqrt{2}$, embora sendo a medida da hipotenusa de um triangulo rectângulo de lados de comprimento unitário, não era um número racional. A sua descoberta, apesar de ser uma elegante descoberta matemática, foi mantida em segredo durante algum tempo no círculo de privilegiados que tinham acesso ao conhecimento.
Apresentamos a seguir o argumento que suporta a evidência de que o número raiz de dois não pode ser obtido como a razão entre dois números inteiros.

> Suponhamos que $\sqrt{2} = \frac{p}{q}$ com $q \neq 0$ e p e q não têm factores comuns. Isto, a ser verdade, implica que
>
> $$p^2 = 2q^2$$
>
> ou seja, diz-nos que p^2 é par e por isso também p tem de ser par, mas se p é par então é da forma $p = 2p'$ e temos também $4p'^2 = 2q^2$ o que implica que $q^2 = 2p'^2$ e portanto também q^2 é par e como consequência q é par. Mas isto significa que p e q têm um factor comum, nomeadamente o 2. Isto contradiz a nossa suposição inicial de que p e q não têm factores comuns, o que nos leva a uma contradição. Concluimos por isso que não existem números inteiros p e q tais que a sua razão seja igual à raiz quadrada de dois, e como tal $\sqrt{2}$ não é um número racional.
>
> — Exemplo clássico de uma prova por contradição

A Scripta-Ingenia assume-se como uma revista de divulgação científica tratando temas da ciência e da tecnologia, cobrindo todas as áreas do saber no domínio das ciências exactas ou aplicadas. Interessa-se ainda por artigos de opinião, sobre tópicos científicos ou não, desde que escritos por autores na área das ciências e da engenharia, e que reflitam as suas opiniões enquanto membros dessa comunidade.

Chief Editor — Nelson Martins-Ferreira
CDRSP-ESTG, IPLeiria

The School of Athens, by Raphael, 1509, at Apostolic Palace, Vatican City

A Escola de Atenas, cujo nome original *Causarum Cognitio* se manteve até ao século XVII, foi inspirada no projecto do grande arquitecto renascentista Donato di Angelo del Pasciuccio (1444-1514), conhecido como Bramante, para a renovação da Basílica de S. Pedro. Na obra, que representa a verdade adquirida através da razão, duas figuras centrais retratam a essência dos pensadores da Antiguidade Clássica e, simultaneamente, o tempo de Rafael: Platão aponta para o céu enquanto segura o seu livro Timeo, ladeado por Aristóteles com a Ética; Pitágoras é representado de lado, de modo a permitir observar a explicação do diatessaron; reclinado nos degraus da escada, Diógenes sugere a leitura; à sua frente, Eráclito, o filósofo pessimista com traços de Miguel Ângelo; à direita, Euclides ensina geometria, Zaratustra segura o Globo Celestial e Ptolomeu o Globo Terrestre, tendo por companhia o próprio Rafael.

Em lugar de a ilustração recorrer às figuras alegóricas, como era hábito nos séculos XIV e XV, convocando o olhar para o infinito, Rafael submete o espaço pictórico às leis do plano, revelando conhecimento da arquitetura dos banhos romanos, fazendo a síntese entre o pagão e o profano. Perante esta composição expansiva, o espectador quase se alheia do facto de o espaço ser mal iluminado.

Dispostas da esquerda para a direita, as solenes figuras de pensadores representam um verdadeiro debate filosófico: astronomia, geometria e aritmética são descritas de forma concreta, num imponente plano arquitectonicamente convergente para o eixo central do espaço abobadado.

in `abrancoalmeida.com/artes/pintura/a-escola-de-atenas`

Self-adjusting orthoses design

by A. PRATES

Centre for Rapid and Sustainable Product Development,
Polytechnic Institute of Leiria, Marinha Grande, Portugal

Abstract: This paper proposes an approach to the development of a customized 3D printed multi-material cervical orthosis that combines new production techniques with smart materials and biomimetic structures. It suggests a lightweight, waterproof, ventilated, hygienic and comfortable orthoses designed specifically for each patient in collaboration with doctors, additive manufacturing specialists and designers. The combination of innovative production techniques with smart materials can generate an enhanced product, whose added value can be perceived by differentiated attributes and applications.

Keywords: Human factor in design, Customized and personalized product development, Smart product engineering.

1 Introduction

Through many years orthoses had no apparent innovation. The traditional manual methods for creating customized orthoses have many drawbacks including the intensive work, time-consuming and imprecise process which may affect the comfort of orthoses and limit treatment quality. Today designers are taking orthoses to another level with the use of forward thinking methods, integrating both innovative technologies and new materials, contributing to a more accurate treatment. There is a large variety of cervical collar orthoses with different characteristics for different clinical indications, of various materials, prefabricated in different sizes. Focusing on the most commonly used cervical collar orthoses and their characteristics and purpose we will explore a new solution of orthosis trough the introduction of novel product development techniques meeting the user's morphology instead of purely adjusting a standard solution.

The integrated methodology approach of medical image processing and reverse engineering can be applied to construct 3D printed models with biomimetic structures and smart printed material/shape memory material which are programmed to respond as desired. In the following sections, these topics are described in detail, referring to the corresponding stage of the development. In general, the result is a 3D printable material that when in contact to the user's body temperature, changes itself into an ergonomic shape. The organic structure is developed based in strategies of growth of the coral reefs.

2 Cervical Collar Orthosis

An Orthosis is an external medical device designed to stabilize, immobilize, prevent deformity, protect against injury, or assist with the function of a body part. The purpose of cervical collar is to alleviate instability of a compromised cervical spine, while being patient-friendly, lightweight and economic. The most commonly used semi rigid cervical collars are the Aspen, Malibu, Miami Jackson, Nec Loc and Philadelphia collars, as pictured in Figure 1.

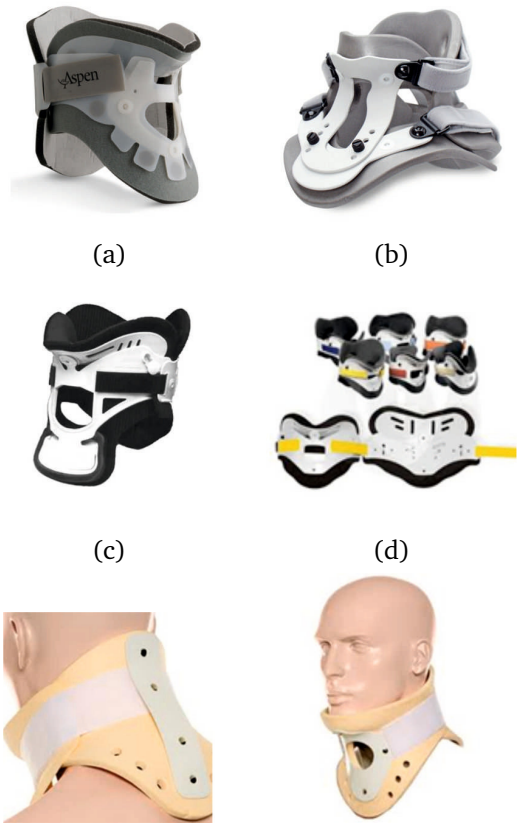

Figure 1 - (a) Aspen; (b) Malibu; (c) Miami Jackson; (d) Nec Loc; (e) and (f) Philadelphia.

There are some known problems usually associated with its use:

- Muscle atrophy
- Heavy
- Odor
- Skin rash or breakdown
- Psychological dependence
- Soft tissue contracture
- Pain
- Lack of hygiene
- Discomfort

The pressure applied in soft tissues and poor circulation is a high risk for developing ischemic wounds and cause of discomfort and pain. The psychological dependence and the sensation of movement or strain of the neck especially in cases when the collar is worn over a longer period of time as well as muscle atrophy, skin friction and facial hair growth in men, should also be considered.

Combinations of rigid and flexible materials in collar types of cervical orthoses are usually the choice to prevent pain. Comfort is also an issue and for that reason cervical motion restriction efficacy is often sacrificed. The more effective ones are frequently more uncomfortable. In general, the cervical orthoses are more effective in restricting the flexion and extension than restricting lateral bending and axial rotation.

The adequacy of the orthosis must be followed whether its purpose is to support, prevent, immobilize or correct the spine. For this matter we will focus only on the first two alternatives. It is also essential to determine the degree of freedom and in which motion of the spine would be controlled, flexion, extension, lateral bending or axial rotation. The rigidity of the components at the chin and the occiput along with the increase of the vertical length, are the main elements in restricting motion.

3 Design Methodologies

When we talk about methodology, we refer to the process that is used to reach a solution. Centered on the virtual model of the patient body and with specific medical data, the main object is to develop a cervical collar with high level of customization in order to satisfy functional requirements and an adequate immobilization or support with maximum comfort and with specific motion control.

Starting from the customer/patient needs and the disadvantages/cons of traditional orthoses and the desirable features for developing a novel orthosis based on medical data, reverse engineering, 3D printing and smart materials, some solutions are explored in order to create a functional, more accurate and comfortable model.

Desirable features:

- Prevent muscle atrophy
- Ventilated
- Lightweight
- Customized
- Waterproof
- Recyclable
- Localized intervention
- Hygienic
- Comfortable

The design intent is building a lightweight, washable, most accurate and ventilated orthosis designed especially for each patient that is both comfortable and functional with particular goals:

The design intent is building a lightweight, washable, most accurate and ventilated orthosis designed especially for each patient that is both comfortable and functional with particular goals:

- to innovate and optimize the product (materials selection, manufacturing, use, end of life)
- to improve custom-fit product process
- to increase the sensation of comfort
- to reduce costs (efficient use of materials)
- to reduce manufacturing times

4 Biomimetic

The combination of 3D technologies and new design inspired in algorithms that mimic patterns and processes in nature, give us new ways of thinking about form, material behavior, structure performance, etc. The main thrust of biomimetics is also to transfer functions, mechanisms and principles from one field to another. Inspired by the algorithmic structures of coral reefs and the systematic exploration of how pattern and form emerge in nature and its strategies of growth, we're interested in using these same rules of growth for design, instead of merely mimicking nature.

A smart material with streching memory effect that when in contact to the user's body temperature, changes itself into an ergonomic shape. Surfaces of multilevel branching fibers with specialized tips that helps reduce the risk of shear and control friction, suggesting a "body's natural (biological) cover". Reduction of the adhesion, using a material inspired in nano filaments of lotus flower with hydrophobic characteristics that allows skin to breath and perspire without getting wet; promotes a more comfortable orthosis.

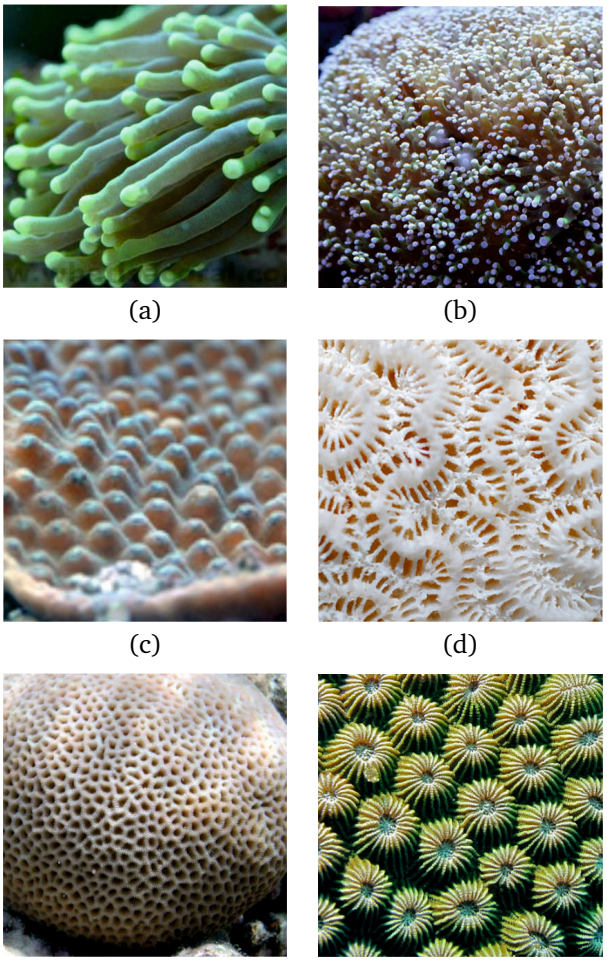

(a) (b) (c) (d) (e) (f)

Figure 2 - (a) Euphyllia glabrescens; (b) Euphyllia paradivisa; (c) Turbinaria sp; (d) Faviidae;(e) Gardineroseris; (f) Diploastrea heliopora.

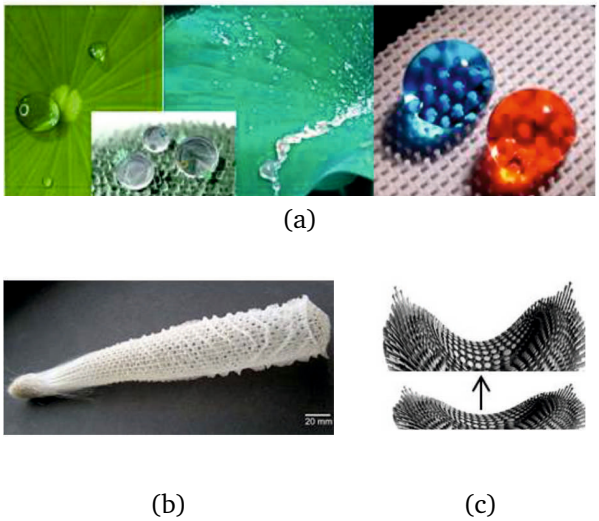

(a) (b) (c)

Figure 3 - (a) Hidrophobic lotus leaf effect; (b) Skeleton of Euplectella sp, showing the lattice-like skeleton of fused siliceous spicules; (c) Stretching memory effect.

The skeletal structure of the glass sponge Euplectella aspergillum displays a remarkable multi-level hierarchical design that gives it superior structural properties. Also in nature we find fractal honeycomb structures which are responsible for excellent stiffness, various patterns and forms with an economic design.

Analyzing this pre-optimized structures from nature and their functional properties we can get to a hyper-structural carcass and a super hydrophobic surface with shape memory material organic behaviour and with material being efficiently applied, only where it is necessary.

5 Customization

Customization of orthoses design can also bridge the gap between personal and technological fields assuming an extension of the user style and personality. Used temporarily or for long periods of time, these medical devices reveal also a social burden of a negative impact.

The negative impact may be reduced when the identity of the user and their lifestyle is reflected, uniting the technological and social aspects. The cervical collar is custom-fit with the ability to adequate the users personality in the design stage. In this phase the user can introduce some personal details in order to change the way he will perceive and relate to the final product without interfering with the functional characteristic of the model.

With the customization of this medical device, we can enhance the therapeutic treatment, having the ability to look at a patient on an individual basis allowing a more accurate diagnosis and specific treatment plan. In this model, the structure will be reinforced in the injury located area and restrain motion where is necessary with higher accuracy, tailored to each individual patient. It is through the diagnostic that is selected the appropriate and optimal treatment based on the context of each patient.

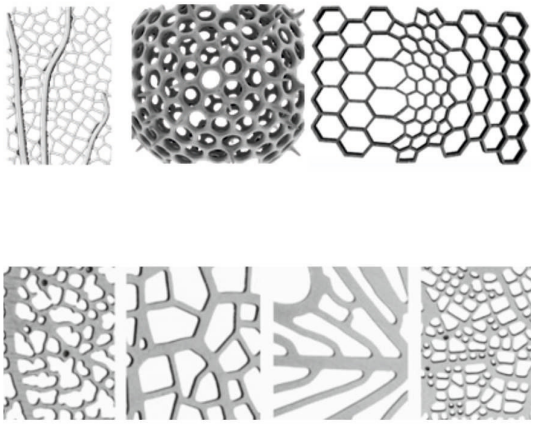

Figure 4 - bioinspired patterns.

6 The development of a new design framework

As indicated, the development of the cervical collar is supported in the patient's treatment plan and the type of lesion to be intervened. This will start at first in the hospital and will end in a custom application orthosis manufactured by 3D printing.

The inner surface of the structure with streching memory effect and hydrophobic characteristic, adapts to the patients neck making it more comfortable, allowing free skin perspiration, as well as the daily hygiene, without requiring removal. The rigid outer structure fulfills its immobilizing function.

The necessary elements for the development of the orthoses can be provided through medical imaging and patient's data identified by the doctor. This can be also complemented through 3D scanning tools.

The CAD / CAM (Computer Aided Design / Computer Aided Manufacture) for orthopedics are a very promising technology. The RX is still the most frequently used exam in cervical trauma. However, the use of CT scan allows rapid acquisition of images in axial and sagittal and coronal reconstructions, although the risks linked with high levels of radiation, that the patients are subjected to.

These are the main steps of the development procedure that can be followed after an injury occurs:

First diagnose in the hospital Identification of the exact injury location by an orthopedist with medical imaging (Figure 5). A computed tomography (CT) scan is an imaging method that uses x-rays to create pictures of cross-sections of the body, typically called slices. Three-dimensional models of the body area can be created by stacking the slices together.

CT scan is saved as a 3D medical data model of affected soft and/or hard tissues.

(a)

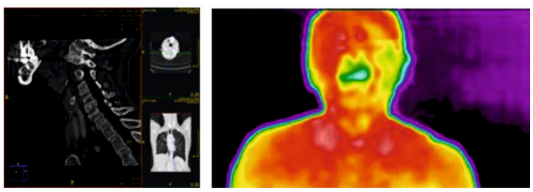

(b)

Figure 5 - Diagnosis.

Digital 3D model Together with medical data, we can reproduce a structure related to the area to be intervened. Through a 3D scanning equipment, it is possible in a few minutes to acquire the patient 3D surface coordinates generating a three-dimensional geometry data. This two approaches can be complementary (Figure 6).

(a)

(b)

(c)

Figure 6 - 3D model.

Development of a pattern structure Directly related to the injury location, following biomimetic principles along with full evaluation by an Orthopedics Doctor, the Additive Manufacturing Technician generates a structure based on medical data and planning, through 3D scanning and 3D modeling tools (Figure 7).

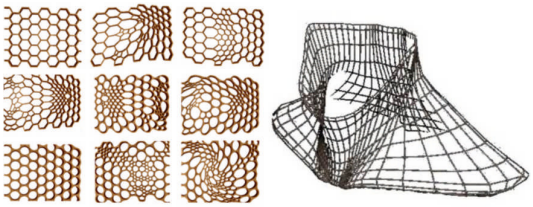

Figure 7 - Bio inspired structure with medical evaluation

Model is sent to multimaterial 3D printer The cervical orthoses will be 3D printed with multi-material. In the inner surface a shape memory and flexible material would continuously optimize its shape in response to the user's body temperature. The outer structure would keep its rigid status so the immobilization occurs making it both effective and comfortable (Figure 8).

(a)

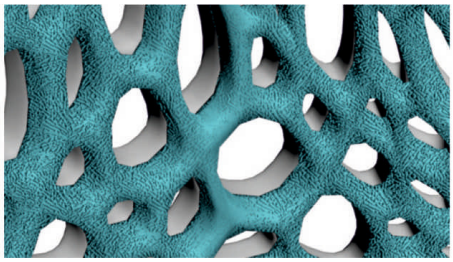

(b)

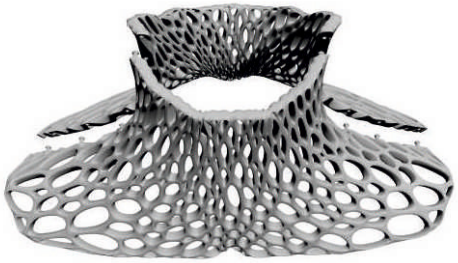

(c)

Figure 8 - AM printing

Application to the patient This custom-made orthoses may be immediately applied to the patient after 3D printed, providing a more accurate and comfortable treatment. The patient will be able to use it throughout personal hygiene routine and won't be concerned with the odor addressed to perspiration being lightweight through every day usage (Figure 9).

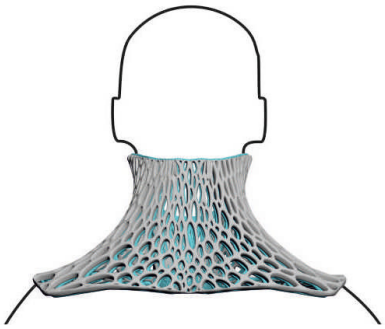

(a)

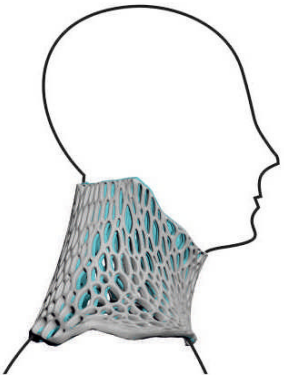

(b)

Figure 9 - Application of final orthosis to the patient

7 Future Work

Nowadays we're living in a manufacturing revolution that promises to change the way we make things. After 3D Printing becoming increasingly accessible and optimized, 4D printing will unquestionably make the difference expanding the boundaries of "making".

The 4D printing concept was initially proposed by Massachusetts Institute of Technology faculty member Skylar Tibbits earlier this year. The 4D printing concept proposed, allows materials to "self-assemble" into 3D structures. The few existing studies are now being developed. These recent studies represent strong advances in additive manufacturing with programmed shaped memory polymer composites using glass fibers.

Last October 2013, researchers at the University of Colorado Boulder have demonstrated the importance of fibers location and orientation within the composite material, in order to determine the degree of shape memory effects like folding, curling, stretching or twisting and the ability to control those effects by heating or cooling the composite material. For future work we intend to integrate into the product development of the cervical orthoses this novel approach and innovative concept.

8 Conclusion

The collaboration and inputs brought into design development starting from medical ground to designers, engineers, manufacturing specialists and the product user itself, can generate an enhanced product. Also the combination of innovative production techniques with smart materials, whose added value can be perceived by differentiated attributes and applications.

References

[1] Academic Journal of Manufacturing Engineering. Tarnita, Daniela et al. 2013. Orthopaedic Prototypes Obtained by 3D Printing Technology, s.l. : Academic Journal of Manufacturing Engineering, 2013, Vol. 11.

[2] Applied Physics Letters. Ge, Qi et al. 2013. Active materials by four-dimension printing, s.l. : AIP Publishing LLC, 2013, Vols. 103, 131901. Beilstein Journal of Nanotechnology. Ensikat, Hans J. et al. 2011. Superhydrophobic in perfection: the outstanding properties of the lotus leaf, s.l. : Beilstein Journal of Nanotechnology, 2011, Vols. 2, 152-161.

[3] Boulder, University of Colorado. 2013. www.colorado.edu. CU-Boulder researchers develop 4D printing technology for composite materials. [Online] 10 22, 2013. [Cited: 10 29, 2013.] www.colorado.edu/news/releases/2013/10/22/cu-boulder-researchers-develop-4D-printing-technology-for-composite-materials.

[4] Clark, Charles R. 2005. The Cervical Spine. USA : Lippincott Williams & Wilkins, 2005. Clinical Prosthetics and Orthotics. White, Augustus A. 1983. Some Comments on Cervical Orthoses, s.l. : Spring C.P.O., 1983, Vols. 7, 3. Coelho, Marcelo. 2013. Hyperform. Marcelo Coelho. [Online] 2013. [Cited: 11 8, 2013.] http://www.cmarcelo.com/#/hyperform/.

[5] ERCIM News. Kruszynski, Chris and Kik, Annete. 2006. Computer measures Coral Structures, s.l. : ERCIM News, 2006, Vols. 66, 52-53.

[6] Evill, Jake. 2013. Cortex. Jakevilldesign. [Online] Dunked, 2013. [Cited: 10 23, 2013.] jakevilldesign.dunked.com/cortex.

[7] Fiabilitate si Durabilitate. Ciobanu, Octavian et al. 2013. The use of 3D scanning and rapid prototyping in medical engineering, s.l. : Academica Brâncusi, 2013, Vols. s.1, 241-247.

[8] Journal of Prosthetics and Orthotic. Lunsford, Thomas R. 1994. The Effectiveness of Four Contemporary Cervical Orthoses in Restricting Cervical Motion, s.l. : Journal of Prosthetics and Orthotic, 1994, Vols. 6, 4, 93.

[9] Journal of Rehabilitation Research and Development. al, Gavin et. 2003. Biomechanical analysis of cervical orthoses in flexion and extesion: A comparison of cervical collars and cervical thoracic orthoses, s.l. : Journal of Rehabilitation Research and Development, 2003, Vols. 40, 6, 527-538.

[10] Journal of Theoretical Biology. Merks, R. et al. 2003. Models of coral growth: spontaneous branching, compactification and the Laplacian growth assumption, s.l. : Journal of Theoretical Biology, 2003, Vols. 224, 153-166.

[11] Research in Engineering Design. Otto, Kevin N. and Wood, Kristin L. 1998. Product Evolution: A Reverse Engineering and Redesign Methology, s.l. : Springer-Verlag London Limited, 1998, Vols. 10, 226-243.

[12] Science. Weaver, JC et al. 2005. Skeleton of Euplectella sp.: Structural Hierarchy from Nanoscale to the Macroscale., s.l. : Science, 2005, Vols. 309, 275-278.

[13] Smart Materials and Structures . Cuevas, J.M. et al. 2012. Shape memory composites based on glass-fibre-reinforced poly(ethylene)-like polymers, s.l. : IOP Publishing Ltd, 2012, Vol. 21.

[14] Soft Matter. Roach, Paul, Shirtcliffe, Neil and Newton, Michael. 2008. Progress in superhydrophobic surface development, s.l. : The Royal Society of Chemistry, 2008, Vols. 4, 224-240. Temas de Reumatologia Clínica. al., Joaquim et. 2009. Órteses para a coluna, s.l. : Moreira JR, 2009, Vols. 10, 2.

[15] Tibbits, Skylar. 2013. TED Talks - Skylar Tibbits: The emergence of "4D printing. http://www.ted.com. [Online] TED Talks, 4 2013. [Cited: 10 22, 2013.] http://www.ted.com/talks/skylar_tibbits_the_emergence_of_4d_printing.html.

Optimization of toolpath trajectories on arbitrary surfaces

by MIGUEL BELBUT GASPAR AND NELSON MARTINS-FERREIRA

Centre for Rapid and Sustainable Product Development,
Polytechnic Institute of Leiria, Marinha Grande, Portugal

Abstract: Given an arbitrary region on the plane, modelled as a graph with a symmetry, we describe a procedure to find the best orientation for slicing, via a zigzag tool-path trajectory based curve, in order to minimize its discontinuities. We also develop some directions on how to generalize the procedure up to the level of optimizing tool-path trajectories on arbitrary surfaces rather than planar regions only.

Keywords: toolpath generation zig-zag strategy optimization additive manufacturing.

1 Introduction

The generation of optimized tool-path trajectories is a demanding and computationally difficult problem that has been considered since the early ages of CAD/CAM systems of rapid prototyping and rapid manufacturing of new products in the area of industry and enterprises in general. Hence it has already been addressed for the last thirty years or so. Nevertheless, the more recent application of 3-D printing, namely to medical application has provided new and challenging problems in this area. The old methods that were already well established are no longer applicable as the technology has moved from the point of view of subtractive manufacturing to additive manufacturing, suggesting new perspectives and strategies of machine toolpath generation. One of the big constraints of this systems is the necessity of a good finishing detail level. In particular it is a heavy handicap the impossibility of always having a continuous toolpath for a whole region at a given layer. We will present some aspect of implementation and optimization for this kind of toolpath generation systems. We will give special attention to the so-called zig-zag strategy, giving some details on how it is modelled and implemented in a computer system, and also on how to optimize the number of discontinuities in the path. These results are already implemented for planar regions but we will also give further indications on how they can be extended to the level of trajectories to cover regions in arbitrary triangulated surfaces. In this text we will also explain how to develop a procedure to automatically generate toolpath trajectories in abstract triangular spaces, with possibly applications to other areas of interest rather that the rapid-prototyping and rapid-manufacturing of products for the industry.

This text is only an extended abstract of a ongoing work. It presents ideas and algorithms that can be implemented in any computational system such as Matlab. It considers the case of tool-path optimization trajectories in arbitrary planar regions defined by a graph with a symmetry, as it is defined in [1]. The trajectories by themselves are generated with an algorithm described in [2]. At the end we give some directions on how to generalize the results for arbitrary surfaces.

2 Establishing the framework

As it is explained in [1], an arbitrary region in the plane may be described as a graph with a symmetry, that is a system (A, B, d, c, φ) in which

$$A \underset{c}{\overset{d}{\rightrightarrows}} B$$

is a directed graph and

$$\varphi\colon A \to A$$

is a bijection such that $d\varphi = c$. As usual, the elements in A are considered as directed edges with an element $a \in A$ pictured as

$$d(a) \xrightarrow{\ a\ } c(a)\ ,$$

and its image by φ considered as the successor directed edge defining the contour of the region

$$d(a) \xrightarrow{\ a\ } c(a) \xrightarrow{\ \varphi(a)\ } c\varphi(a)\ ,$$

with the assumption that its interior is always on the left.

For practical purposes we give a specific example which will be used throughout the text to illustrate the several steps involved in the outlined procedure.

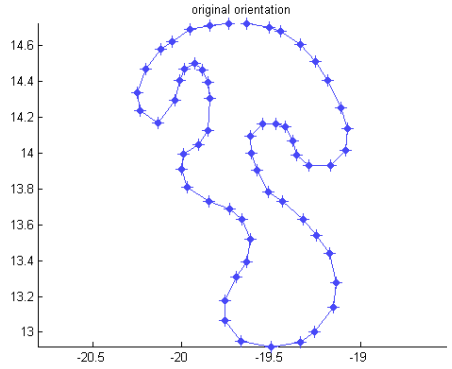

Fig. 1 - Original curve orientation.

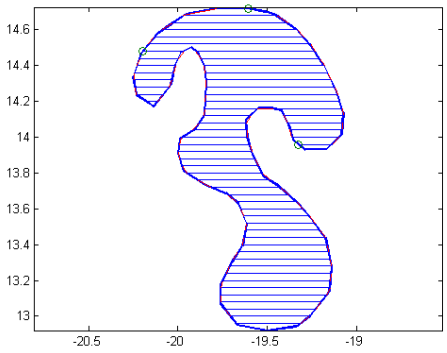

Fig. 2 - Zig-zag toolpath trajectories.

The example is depicted in Figure 1 above and it is defined by the following data, presented as a sequence of directed edges, each one determined by its endpoints, encoded in a vector named P. In other words, we have a set $A = \{1, 2, 3, \ldots, 58, 59\}$, and a set $B \subset \mathbf{R}^2$. The vector P is displayed as:

```
P =
   −19.3566,  13.9876
   −19.2874,  13.9291
   −19.1665,  13.9291
   −19.0801,  14.0168
   −19.0719,  14.1372
   −19.1089,  14.2534
   −19.1829,  14.4065
   −19.2515,  14.5121
   −19.3360,  14.6071
   −19.4487,  14.6820
   −19.5121,  14.7039
   −19.6388,  14.7259
   −19.7368,  14.7259
   −19.8404,  14.7113
   −19.9556,  14.6893
   −20.0536,  14.6235
   −20.1169,  14.5797
   −20.2033,  14.4700
   −20.2494,  14.3385
   −20.2321,  14.2361
   −20.1342,  14.1703
   −20.0363,  14.2946
   −20.0132,  14.4042
   −19.9853,  14.4698
   −19.9246,  14.5015
   −19.8824,  14.4645
   −19.8507,  14.3959
   −19.8402,  14.3062
   −19.8507,  14.1267
   ...
   ...
   −19.9035,  14.0475
   −19.9880,  13.9947
   −19.9985,  13.9102
   −19.9672,  13.8121
   −19.8462,  13.7317
   −19.7310,  13.6879
   −19.6619,  13.6294
   −19.6158,  13.5197
   −19.6388,  13.3955
   −19.6964,  13.3077
   −19.7598,  13.1762
   −19.7598,  13.0665
   −19.6676,  12.9496
   −19.5006,  12.9203
   −19.3335,  12.9423
   −19.2586,  13.0007
   −19.1492,  13.1396
   −19.1377,  13.2785
   −19.1722,  13.4393
   −19.2471,  13.5417
   −19.3220,  13.6294
   −19.4372,  13.7317
   −19.5179,  13.7829
   −19.5812,  13.9072
   −19.6100,  14.0022
   −19.6158,  14.0972
   −19.5467,  14.1630
   −19.4718,  14.1630
   −19.4199,  14.1484
   −19.3796,  14.0680
```

The maps d, c are, respectively, the first and second components, while the map φ is defined by $\varphi(i) = i+1$ if $i \leq 59$ and $\varphi(59) = 1$. The maps d and c may be also seen in terms of the vector P as $d(i) = P(i, 1)$, $c(i) = P(i, 2)$.

In the next section we assume a vector such as P is defined and will deduce a collection of possible orientations which minimize the tool-path trajectories, as exemplified in Figure 2.

3 Finding the best orientation for slicing

Given P as before, we want to minimize the number of inflection points for a scan angle θ. The algorithm is described in pseudo-code, using Matlab syntax.

```
Input: P – n–by–2, polygon's vertices as
rows (x,y)
Output: Aopt – m–by–2, m ranges (amin,amax)
of optimal angles.

% convert to complex form
Pc=P*[1;i];

% Obtain the orientation of each edge:
A=angle(Pc([2:end,1])–Pc)*180/pi

% Get inner angles
IA=mod(mod(180–A,360)+mod(A([2:end,1]),360)
    ,360);
```

We are interested in the concavities, i.e, `IA>180`. At a convex vertex, as the scan slope passes the emerging edge's slope, that vertex ceases to be an inflection point. At the same time, the next vertex becomes a new inflection point, if it is convex, too. So as this scanning slope is reached, no new net inflection points are added. Something different occurs when we consider concave vertices: as we reach the emerging edge's slope, a new inflection point appears (in fact, two).

When two successive vertices are concave, no net inflection point is added, either.

```
% Concave vertices:
CC=IA>180

% Changes, that is, sequences convex–>concave
% This is the non–trivial difficult part
DC=diff(CC([end,1:end]))

% Sort the angles (mod 180):
A3=sortrows([mod(A,180), DC])
```

By cummulative sum of the net change in number of inflection points, we find the range of theta with the minimum amount of infl. points:

```
A4=[A3(:,1), cumsum(A3(:,2))]

% Extract the needed information:
ixm=find(A4(:,2)==min(A4(:,2)));

tmp=[ixm-ixm([end,1:end-1]),...
     ixm([2:end,1])-ixm]~=1
ixm=[ixm(tmp(:,1)),ixm(tmp(:,2))]
AOpt=[A4(ixm(:,1),1),A4(ixm(:,2),1)]
```

The result of each of the preceding steps applied to the input data P as defined in the previous section is presented at the end.

The output result is presented as ranges of angles in the form

```
ang_min1, ang_max1;
ang_min2, ang_max2;
...
ang_mink, ang_maxk
```

which for the working example has the following result.

```
AOpt =
         0   27.5592
  159.1581  170.1824
```

This means that for rotations with an angle between 0 and 27.5592 degrees, there are a minimum number of discontinuities in the tool-path trajectory. For rotation angles ranging from 27.5592 to 159.1581 degrees, the number of discontinuities is increasing while it again attends a minimum when the rotation angle is between 159.1581 and 170.1824. Again form 170.1824 to 360 there is a larger number of discontinuities.

The suggested optimal angles are displayed in the following pictures.

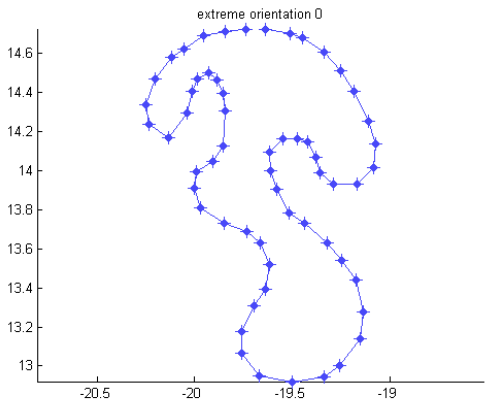

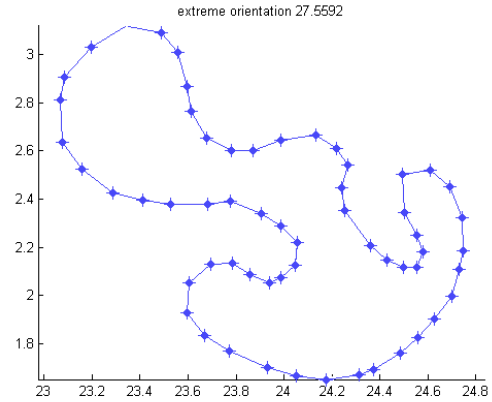

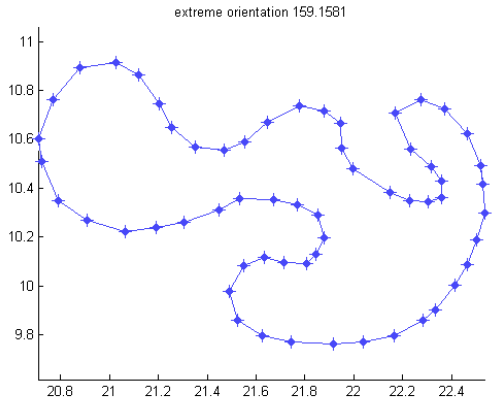

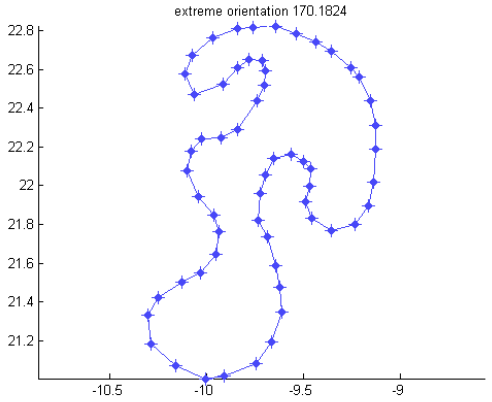

4 Conclusion

To conclude we remark that the procedure may be generalized to the context where the region is not necessarily planar but is embedded into an arbitrary surface in the space. This is important for the purpose of generating tool-path trajectories for rapid manufacturing and rapid prototyping since it will allow a greater number of applications. To to that we will only need to transform the structure used in [2] by imposing that the linking lines between two intersected points in the same g-component, to use the nomenclature of [2], are no longer straight lines but are geodesic path instead. This part is not yet implemented. It will use algorithms for working with

geodesic paths and then combine the structure (E, r, g, s) used in [2],requiring also the geometric information concerning the convexity of each edge, used in here, obtaining thus the same results for surfaces.

References

[1] Gaspar, Miguel Belbut, and Nelson Martins-Ferreira. *A procedure for computing the symmetric difference of regions defined by polygonal curves*, Journal of Symbolic Computation **61** (2014) 53–65.

[2] Miguel Belbut Gaspar, Nelson Martins-Ferreira, *Sobre estratégias de varrimento contínuo para o preenchimento de regiões arbitrárias no plano*, Boletim da Sociedade Portuguesa de Matemática (2010), no. Especial, 78–86.

Appendix

Below is presented the output of each relevant step in the execution of the procedure described in the text. Each vector is listed from top to bottom and from left to right and from one page to the next one.

```
A =              -90.0000   106.8612   123.0239   -33.8943
                 -51.7612    93.4688   131.6335    51.7612
 -123.6901        -9.9282    43.5840   146.3987    78.1326
 -147.9946         7.4788           0  160.9096    66.9420
  -97.1250        37.9872   -15.7485   170.1824    27.5592
  -72.2576        51.7612   -63.3678   180.0000   -41.1859
  -33.6127        85.2582   -74.0102  -171.9742   -65.2249
  -20.8419       102.1292   -40.2314  -169.2226   -83.2902
  -40.2314       126.1941           0  -146.1057   -93.3665
  -67.2041       130.4869    45.4323  -145.3096
 -100.5043       138.3852    86.1050  -128.2388
 -123.2922       147.6048   107.7053  -109.3018
 -115.7139       117.0168   115.7693   -80.4154
```

```
CC =             1     1     1     1     0
                 1     1     1     1     0
      0          1     0     1     1     0
      1          1     0     1     1     0
      1          1     0     1     1     0
      1          1     0     1     1     0
      1          1     0     1     1
      0          1     0     1     1
      0          1     0     1     1
      0          1     0     1     1
      0          1     1     1     0
```

```
DC =             1     0     0     0     0
                 0     0     0     0     0
      0          0    -1     0     0     0
      1          0     0     0     0     0
      0          0     0     0     0     0
      0          0     0     0     0     0
      0          0     0     0     0
     -1          0     0     0     0
      0          0     0     0     0
      0          0     0     0     0
      0          0     1     0    -1
```

```
A3 =
         0         0
         0         0
         0         0
    7.4788         0
    8.0258         0
   10.7774         0
   27.5592         0
   32.0054    1.0000
   33.8943         0
   34.6904         0
   37.9872         0
   43.5840         0
   45.4323         0
   51.7612         0
   51.7612         0
   51.7612         0
   56.3099         0
   56.7078    1.0000
   64.2861         0
   66.9420         0

   70.6982         0
   78.1326   -1.0000
   79.4957         0
   82.8750         0
   85.2582         0
   86.1050         0
   86.6335         0
   90.0000         0
   93.4688         0
   96.7098         0
   99.5846         0
  102.1292         0
  105.9898    1.0000
  106.8612         0
  107.7053         0
  107.7424         0
  112.7959         0
  114.7751         0
  115.7693         0
  116.6322         0
  117.0168         0

  123.0239         0
  126.1941         0
  128.2388         0
  130.4869         0
  131.6335         0
  138.3852         0
  138.8141         0
  139.7686         0
  139.7686         0
  146.1057         0
  146.3873         0
  146.3987         0
  147.6048   -1.0000
  159.1581   -1.0000
  160.9096         0
  164.2515         0
  170.0718         0
  170.1824         0

A4 =    0         0   70.6982    2.0000  117.0168    2.0000
         0         0   78.1326    1.0000  123.0239    2.0000
         0         0   79.4957    1.0000  126.1941    2.0000
    7.4788         0   82.8750    1.0000  128.2388    2.0000
    8.0258         0   85.2582    1.0000  130.4869    2.0000
   10.7774         0   86.1050    1.0000  131.6335    2.0000
   27.5592         0   86.6335    1.0000  138.3852    2.0000
   32.0054    1.0000   90.0000    1.0000  138.8141    2.0000
   33.8943    1.0000   93.4688    1.0000  139.7686    2.0000
   34.6904    1.0000   96.7098    1.0000  139.7686    2.0000
   37.9872    1.0000   99.5846    1.0000  146.1057    2.0000
   43.5840    1.0000  102.1292    1.0000  146.3873    2.0000
   45.4323    1.0000  105.9898    2.0000  146.3987    2.0000
   51.7612    1.0000  106.8612    2.0000  147.6048    1.0000
   51.7612    1.0000  107.7053    2.0000  159.1581         0
   51.7612    1.0000  107.7424    2.0000  160.9096         0
   56.3099    1.0000  112.7959    2.0000  164.2515         0
   56.7078    2.0000  114.7751    2.0000  170.0718         0
   64.2861    2.0000  115.7693    2.0000  170.1824         0
   66.9420    2.0000  116.6322    2.0000

tmp =
     1     0
     0     0
     0     0
     0     0
     0     0

     0     0
     0     1
     1     0
     0     0
     0     0
     0     0
     0     1

ixm =
     1     7
    55    59
```

Produção de peças biodegradáveis de parede fina por injeção

by C. Santos, A. Mendes, P. Carreira, A. Mateus & N. Alves

Centre for Rapid and Sustainable Product Development
Polytechnic Institute of Leiria, Marinha Grande, Portugal

Resumo: Actualmente, a indústria dos moldes para responder às exigências do mercado procura diversificar os seus mercados, apostando em produtos diferenciados e de valor acrescentado. Foi neste sentido que se desenvolveu o projecto de concepção e fabrico de vasos biodegradáveis para germinação de plantas.

O objectivo deste artigo de investigação passa pela concepção e desenvolvimento de um vaso para germinação de plantas produzido em material biodegradável. A validação do projecto desenvolvido para uma peça de paredes finas em material biodegradável, foi realizada através da fabricação da ferramenta (molde) e o processamento de peças (vasos biodegradáveis).

Este estudo demonstrou-se promissor como pilar de apoio para o desenvolvimento de futuros produtos em materiais biodegradáveis de paredes finas, obtidos pelo processo de injecção de termoplásticos. Os resultados alcançados permitiram validar o processo desenvolvido, bem como o produto obtido de paredes finas em material biodegradável, que neste caso foi um vaso biodegradável para germinação de plantas.

Palavras-chave: Polímeros biodegradáveis, vasos de plantas, injecção de termoplásticos, paredes finas.

1 Introdução

O processo de injecção de termoplásticos, por imposição do mercado, tem sido alvo nas últimas décadas de avanços tecnológicos no desenvolvimento de moldes para peças cada vez mais complexas com um rigor dimensional cada vez mais apertado, no entanto, estudos direccionados na área do desenvolvimento de peças de paredes finas obtidos em polímeros biodegradáveis, não são muito correntes.

Embora seja um tema da actualidade, a acessibilidade a uma correcta selecção de polímeros biodegradáveis não é comum, não existindo ainda uma produção em grande escala deste género de formulações (que nalguns casos têm que ser adequadas a cada caso e ambiente biológico). Estas formulações geralmente são constituídas por um polímero sintético (como um poliéster) e um polímero natural como o amido. Este trabalho de investigação visa resolver o problema da utilização de vasos de plantas tradicionalmente utilizados, através do desenvolvimento de uma estratégia envolvendo a injecção de um polímero biodegradável.

1.1 Estudo do mercado

O aumento do preço do petróleo, tem conduzido nos últimos anos à intensificação de projectos de investigação, visando a obtenção de produtos alternativos aos plásticos convencionais. Ultimamente, os plásticos biodegradáveis, começarem a ser produzidos para uso industrial e comercial, deixando de ser apenas utilizados para fins de investigação [1]. As perspectivas mais optimistas apontam para um aumento da capacidade mundial de produção de bioplásticos de 0,36 milhões de toneladas (em 2007), para 4,40 milhões de toneladas (em 2020) tal como se indica na Figura 1. Mesmo num cenário mais pessimista, a produção mundial será em 2020 de 1,47 milhões de toneladas.

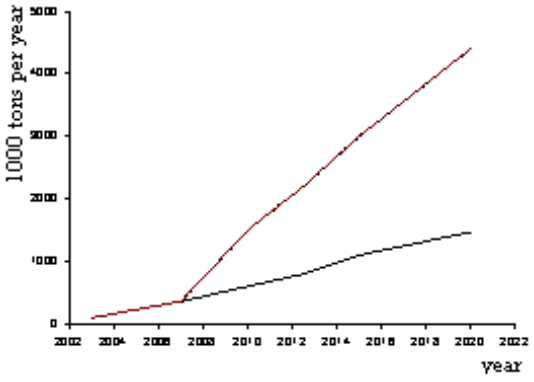

Figura 1 – Projecção da capacidade de produção mundial de bioplásticos até 2020 [1].

Os produtos mais importantes em termos dos volumes de produção em 2007, foram os plásticos de amido (0,15 milhões de toneladas) e o ácido poliláctico (PLA) (0,15 milhões de toneladas). Prevê-se que os bioplásticos mais importantes em 2020 sejam: Plásticos de Amido (1,3 milhões de toneladas); PLA (0,8 milhões de toneladas); PE bio-base (0,6 milhões de toneladas) e PHA (0,4 milhões de toneladas) [1]. O preço de venda dos bioplásticos, constitui ainda o principal obstáculo à penetração destes materiais no mercado, sendo que em média o granulado

de plástico biodegradável apresenta um preço 50% superior ao plástico convencional (PP, PE, PET). No entanto, entre 1990 e 2002 houve um grande aumento da procura de bioplásticos, tal como se indica na Figura 2. Tal deve-se em parte ao aumento do preço do petróleo, diminuição dos custos de produção e implementação de políticas ambientais [2].

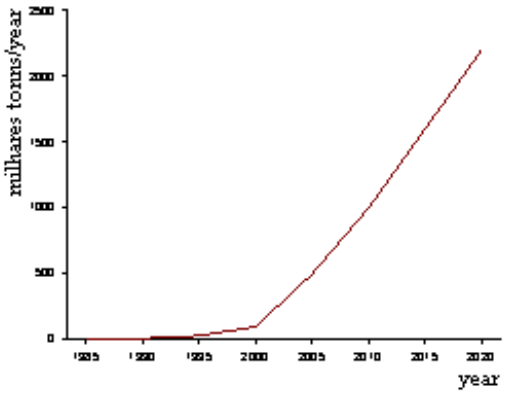

Figura 2 – Previsão da evolução do consumo de bioplásticos [2].

2 Materiais e métodos

2.1 Materiais

Para a moldação por injecção dos recipientes biodegradáveis, foi seleccionado um composto comercial biodegradável. Para tal, foram efectuadas diversas pesquisas sobre os materiais existentes no mercado. Da pequena gama de materiais termoplásticos biodegradáveis encontrados a escolha recaiu sobre o Bioplast GS 2189 da BIOTEC. Comercialmente disponível, e particularmente adaptado à fabricação de produtos injectados alimentares, não alimentares e totalmente biodegradáveis.

2.2 Propriedades do material

O material é apropriado para obtenção de peças pelo processo de moldação por injecção, sendo esta, a técnica de processamento utilizada. Para além desta importante característica, este material é um substituto para o PP (polipropileno), que é o material usualmente utilizado para a produção dos actuais vasos.

Nas Tabelas 1 e 2 são apresentadas as principais propriedades físicas e mecânicas do material seleccionado.

Tabela 1 – Propriedades mecânicas do material.

Propriedades mecânicas	Valor
Alongamento [%]	10–30
Resistência à tracção [MPa]	30–45

Tabela 2 – Propriedades físicas do material.

Propriedades físicas	Valor
Dimensão do granulado [mm]	2.0 – 3.0
Densidade [g/cm3]	1.2 – 1.4
Densidade do fundido [g/cm3]	1.1 – 1.3
Índice de fluidez (190 °C, 2.16 kg)[g/10 min.]	15 – 40
Quantidade de água [%]	< 0.2

2.3 Técnica de Processamento - Injecção de Termoplásticos

Os vasos foram obtidos através do processo de injecção de termoplásticos, sendo de destacar a exigência tecnológica ao nível da moldação de peças plásticas em material biodegradável de paredes finas, que caracteriza o presente estudo. Os testes de injecção foram efectuados nos laboratorios de Engenharia Mecânica do Instituto Politécnico de Leiria. A máquina de injecção utilizada para o processamento dos vasos biodegradaveis foi uma INAUTOM Euro Inj D-80 horizontal (Figura 3).

Tabela 4 – Principais características de máquina de injecção (EURO IN J Série D-80).

	Propriedades físicas	Valor
Sistema de injecção	Diâmetro do fuso [mm]	36
	Relação L/D	20
	Volume injecção [cm3]	183
	Peso injecção [g]	164
	Pressão [bar]	1722
Sistema de fecho	Força de fecho max. [ton]	80
	Max. curso abertura [mm]	320
	Expes. Molde min. [mm]	130
	Expes. Molde Max. [mm]	400
	Abertura Max. [mm]	720
	Espaço entre colunas [mm]	360×360
	Diâmetro de colunas [mm]	60
	Max. Força extractor [ton]	2.74
	Max. Curso extractor [mm]	90

Figure 3 – Thermoplastic injection machine EURO D-80 Inj.

2.4 Projecto e Fabrico do Molde

O bom desempenho de um molde de injecção está directamente associado ao cuidado com o projecto e fabrico de molde. No projecto de molde foram tidas em conta as características da máquina de injecção, designadamente a distância entre colunas, a força de fecho, abertura do molde bem como a capacidade de injecção. A estrutura do molde deve ser suficientemente resistente de modo a suportar os esforços originados durante a injecção. Apesar da peça (vaso biodegradável), ser simples em termos de geometria, é necessário ter em atenção as paredes finas, que caracterizam o produto nos materiais biodegradáveis.

2.5 Modelo CAD do vaso

O modelo CAD do vaso (Figura 4), foi obtido após diversos estudos de mercado e levantamento de patentes, que permitiu a definição das suas funcionalidades. A espessura da peça foi um factor importante, havendo a necessidade da peça ser o mais fino possível (por questões de custo e taxa de degradação), mantendo as suas propriedades estruturais.

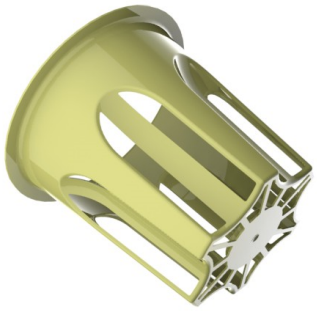

Figura 4 – Modelo CAD da peça.

O uso de espessuras de parede uniformes em toda a peça irá minimizar, deformações, tensões residuais e melhorar o enchimento do molde. Minimizando a espessura da parede da peça, garante-se um melhor arrefecimento e tempos de ciclo. Tudo isto, minimiza o custo final da peça.

2.6 Projecto do molde

A simulação computacional do enchimento da peça foi efectuada no software Moldflow Insight. A simulação serviu de apoio ao desenho, fabrico do molde e de apoio na fase de parametrização da máquina de injecção para processamento dos vasos.

O molde projectado para injecção dos vasos biodegradáveis é um molde de injecção convencional, ou seja um molde de canais frio de cavidade única e foi desenhado no software de modelação TopSolid.

A estrutura do molde é constituída por dois conjuntos principais de placas e calços. O conjunto da bucha (Figura 5) define a parte interior da peça. Por outro lado, o conjunto da cavidade (Figura 6) define a forma exterior da peça.

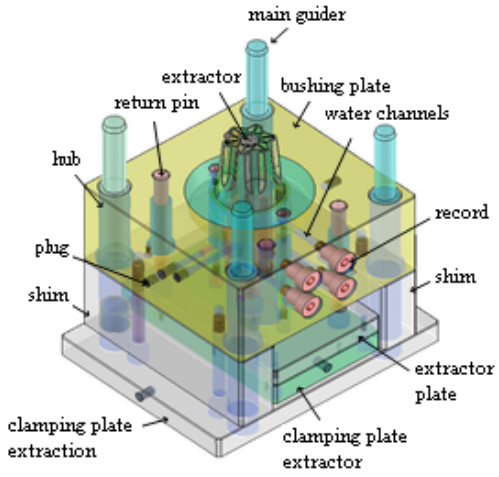

Figura 5 – Parte móvel do molde (bucha).

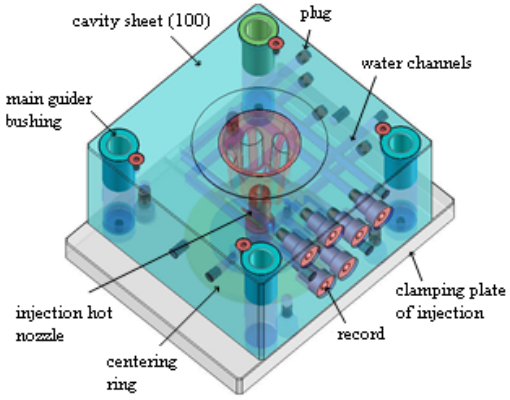

Figura 6 – Parte fixa do molde (cavidade).

O bico de injecção seleccionado, foi um bico quente da THERMOPLAY de referência DN 18046-A-1-1. A opção de se utilizar um bico quente resultou do facto da peça injectada ser de paredes finas em material biodegradável. Uma das vantagens da utilização deste tipo de bico, reside na eliminação do canal de injecção, permitindo a injecção directa sobre a peça. A eliminação do canal de injecção, é importante quando se injecta material de fácil degradação, como é o caso do material considerado neste trabalho de investigação.

3 Resultados

Posteriormente, ao teste do molde, e efectuadas pequenas alterações no polimento de algumas faces e outros pequenos ajustes no molde, iniciou-se a produção dos vasos biodegradáveis. Previamente ao inicio da injecção do material, ainda se testou o funcionamento correcto da extracção, abertura e fecho do molde. Com material pré-processado (em granulado), na tremonha, e material no estado fundido no fuso, deu-se inicio a primeiras injecções de material no interior do molde. Para os parâmetros iniciais tiveram-se em conta as simulações reológicas. Cada ciclo de injecção teve aproximadamente 10 segundos.

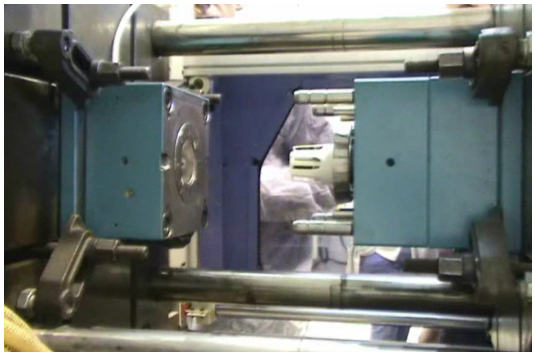

Figura 7 – Injecção dos vasos.

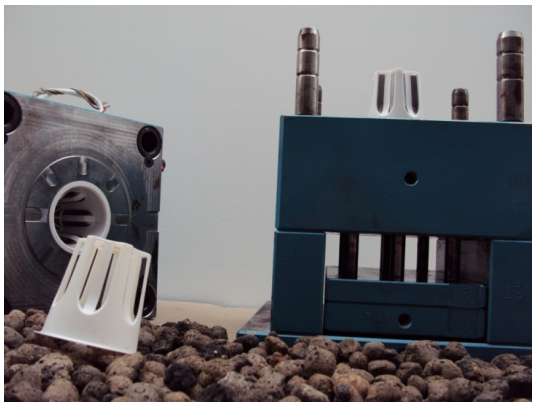

Figura 8 – Molde e vasos biodegradáveis.

4 Conclusão

Num próximo artigo apresentar-se-á sob forma mais detalhada a caracterização do polímero biodegradável, a influência do processamento sobre este bem como o processo de biodegradação do vaso em diferentes solos. O invento em causa encontra-se em fase de conversão a pedido definitivo de Patente Nacional nº 104476.

Figura 9 – Conceito desenvolvido.

Agradecimentos

Os Autores agradecem ao Sr. Paulo Ribeirinho e ao Sr. José Metelo pelo enorme contributo no desenvolvimento deste projecto de investigação.

References

[1] Shen, Li, Haufe, Juliane e Patel, Martin K. 2009. Product overview and market projection of emerging bio-based plastics . PRO - BIP . 2009.

[2] Pradella, José Geraldo da Cruz. 2006. Biopolímeros e Intermediários químicos. Brasil : Centro de Gestão e Estudos Estratégicos, 2006. Relatório Técnico nº 84 396-205.

[3] Falcone, Daniele M. B., Agnelli, José Augusto M. e Faria, Leandro I. L. 2007. Panorama Setorial e Perspectiva na Área de Polímeros Biodegradáveis. Polímeros: Ciência e Tecnologia, 2007, Vols. 17, nº 1, pp. 5 - 9.

Electric Gap Control in a Semiconductor

by M. C. SANTOS AND E. LORA DA SILVA

Department of Physics, University of Coimbra, Portugal
Department of Chemistry, University of Bath, UK

Abstract: We show that the Bi-Layer Graphene allows the control of its electronic gap under an applied voltage.

Keywords: Semiconductor, carbon allotropes.

1 Carbon Allotropes Double Layer Graphene

Many properties of single-layer graphene has been theoretically studied to allow further characterization of this material. These properties are unconventional due to the unique band structure of graphene, which is described in terms of Dirac fermions.

The experimental study of graphene triggered a growing attention to its electronic properties,[14] because the honeycomb lattice defines a band structure [19] with two nodal points in the Brillouin zone which determines a relativistic Dirac-type electronic dynamics [18] (creating links with certain theories of particle physics). These properties are responsible for unusual phenomena, such as the fractional Hall effect,[13, 20, 7, 16] which allows the possibility for magnetic catalysis of an excitonic gap,[6, 5, 10, 9, 8, 11] ferromagnetism and superconductivity. [12]

Other studies related to suspended graphene vacuum, revealed that graphene can change from a semi-metal into an insulator, due to the formation of a gap in the fermionic spectrum, resultant from the chiral symmetry breaking; condensate (exciton). [2, 1]

More recently, attention has turned to the multi-layer graphene [3] and, particularly, to the bi-layer graphene, which also reveals abnormalities, i.e., on the of Quantum Hall effect.[15] In fact, it was shown that the bi-layer graphene also shows unconventional behaviour in its properties, however, these properties are different from those observed in the single-layer of graphene.

There are two main reasons that explain the unconventional physics of multi-layered graphene:

1. The coupling between the layers is relatively weak and therefore some of the properties of the base material, the single layer of graphene, are manifested.

2. The peculiar geometry resulting from the A-B layer stacking (*Bernal stacking*), implies that the connection between the plans takes place mostly in one of the sub-lattices of each plan.

As in the case of the single-layer graphene, also the bi-layer graphene is sensitive to the inevitable disorder generated by environment of the SiO_2 substrate.

It has been theoretically and experimentally shown that the bi-layer graphene is the only material with semiconductor properties, with which the width of the electronic gap is proportional to an applied electric field.

2 Electric-Bias Control in Double Layer Graphene Electronic Gap

We will start start by describing the pure bi-layer graphene system with Bernal stacking, where we only consider the $t_\perp$ coupling amplitude between vertical layers restricted to shorter vertical distances of these carbon atoms. We apply between these planes the electric field f. The Fermi operators are represented in the second-quantization formalism as a Fourier transform of the n on-site operators $a_{\mathbf{n}}$

$$a_{\mathbf{k},j} = N^{-1/2} \sum_n e^{-\imath \mathbf{k}\cdot\mathbf{n}} a_{\mathbf{n},j} \tag{1}$$

which represent plane wave states with $\mathbf{k}$ moment, the indices j are related to four types of sites in the lattice and, N is the number of cells in a layer - see fig. 1. A $4-$spinor is formed as

$$a^\dagger_{\mathbf{k}} = \left(a^\dagger_{\mathbf{k},1}, a^\dagger_{\mathbf{k},2}, a^\dagger_{\mathbf{k},3}, a^\dagger_{\mathbf{k},4}\right) \tag{2}$$

and where the unperturbed Hamiltonian is presented as

$$H_0 = \sum_{\mathbf{k}} a^\dagger_{\mathbf{k}} \hat{H}_0 a_{\mathbf{k}} \tag{3}$$

with matrix

$$\hat{H}_0 = \begin{pmatrix} f & t_\perp & \gamma_{\mathbf{k}} & 0 \\ t_\perp & -f & 0 & \gamma^*_{\mathbf{k}} \\ \gamma^*_{\mathbf{k}} & 0 & f & 0 \\ 0 & \gamma_{\mathbf{k}} & 0 & -f \end{pmatrix} \tag{4}$$

where $\gamma_{\mathbf{k}} = t \sum_{\boldsymbol{\delta}} e^{\imath \mathbf{k}\cdot\boldsymbol{\delta}}$ is related to the in-plane hopping amplitude t, where the sum is performed over the vectors $\boldsymbol{\delta}$, connecting the nearest neighbours of the n sites.

In the Dirac points, $\mathbf{K} = (0, 4\pi/3\sqrt{3}a)$, and $-\mathbf{K}$, the function $\gamma_{\mathbf{k}}$ vanishes. This result occurs in the vicinity of $\mathbf{K}$: $\mathbf{q} = \mathbf{k} - \mathbf{K}$, is linear: $\gamma_{\mathbf{k}} \approx \hbar v_F(q_x - iq_y)$, where $v_F = 3ta/2\hbar$ (with v_F being the Fermi velocity, $v_F = c/300$, c the velocity of light in vacuum, and $\hbar$ the reduced Planck constant).

After diagonalizing the matrix, eq. 4, we obtain:

$$H_0 = \sum_{\mathbf{k}} \Big[\varepsilon_{\mathbf{k},1} \left(\alpha^{\dagger}_{\mathbf{k},1}\alpha_{\mathbf{k},1} - \alpha^{\dagger}_{\mathbf{k},2}\alpha_{\mathbf{k},2} \right) + + \varepsilon_{\mathbf{k},2} \left(\alpha^{\dagger}_{\mathbf{k},3}\alpha_{\mathbf{k},3} - \alpha^{\dagger}_{\mathbf{k},4}\alpha_{\mathbf{k},4} \right) \Big] \quad (5)$$

and the eigenvalues are:

$$\varepsilon_{\mathbf{k},1} = \sqrt{\frac{t_\perp^2}{2} + f^2 + |\gamma_{\mathbf{k}}|^2 + \sqrt{\frac{t_\perp^4}{4} + |\gamma_{\mathbf{k}}|^2(t_\perp^2 + 4f^2)}}$$

$$\varepsilon_{\mathbf{k},2} = \sqrt{\frac{t_\perp^2}{2} + f^2 + |\gamma_{\mathbf{k}}|^2 - \sqrt{\frac{t_\perp^4}{4} + |\gamma_{\mathbf{k}}|^2(t_\perp^2 + 4f^2)}}. \quad (6)$$

and thus represent the electronic dispersion law for the bi-layer graphene (see fig. 2).

Based on the demonstrated results, and schematically shown in fig. 2, an electric-bias increases the electronic band-gap; this behaviour shows that this material has a variable electronic gap dependant on the applied electric field.

3 Effect of Impurities

Based on the above demonstrated results, it is interested to study the impurity effects on the spectrum rearrangement for the bi-layer graphene system.

As observed on other semiconductors with relevant technological impact, impurity effects are decisive for the reliability of the electronic performance of the bi-layer graphene. Impurities and/or dopants are sometimes inevitable during the growth or the processing of the materials. Considerable effort has hence been directed toward the study of defects in semiconductors and insulators and how these can affect device properties and reliability. Much of the present-day engineering of materials consists of pragmatic strategies of trying to control defect densities by processing control and annealing. [17]

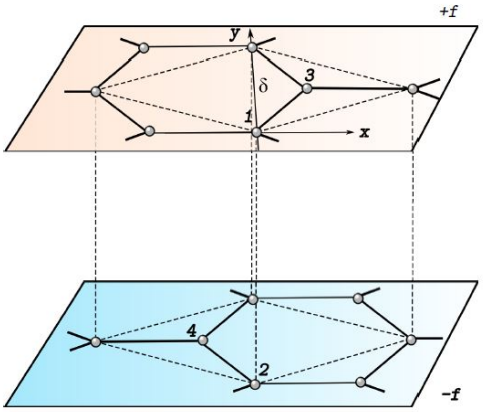

Figure 1. Bernal stacking for the structure of bi-layer graphene. The ±f potential results in the application of an electric field between two layers.

The uncontrolled presence of defects may cause unreliability, being the main source for electrical failure and breakdown of the material. Trapped charges in defects causes a shift in the gate threshold voltage of the transistor; it can also change with time, shifting the threshold voltage with time, thus leading to instability of operating characteristics. Also, trapped charge scatters carriers in the channel and lowers the carrier mobility. [17]

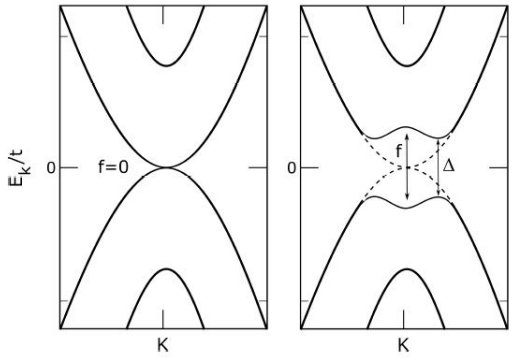

Figure 2. The band structure of bi-layer graphene. When there is no applied electric field, f = 0, the structure is a gapless semi-conductor, but when an electric field is applied, f ≠ 0, the system becomes insulator, and the width of the electronic gap Δ is controlled by the applied field f.

Among such defects are impurities, such as interstitial hydrogen, that can be unintentionally incorporated during the growth environment.[4] Source gases contain hydrogen as carrier gas and in molecular beam epitaxy hydrogen is the prevailing background impurity, exhibiting complex behaviours when introduced in materials. [4]

4 Density Functional Theory Calculations of Bi-layer Graphene

In density functional theory (DFT) [21] the electronic orbitals are solutions of a set of Schrödinger-like equations, referred to as Kohn-Sham equations, from which potential terms depend on the electron density. The Kohn-Sham method assumes that, for each interacting ground state density $n(\vec{r})$, there is a non-interacting electron system with the same ground state density. The interacting ground state is thus obtained through the solution of the Kohn-Sham equations that have the form of the single-particle Schrödinger equation

$$\Big[-\frac{\nabla^2}{2}+v_{\text{KS}}[n(\vec{r})]\Big]\varphi_i(\vec{r})=\epsilon_i\varphi_i(\vec{r}),$$

where v_{KS} is the Kohn-Sham potential, with a functional dependence on the electronic density, n, which is defined in terms of the Kohn-Sham wave-functions by $n(\vec{r}) = \sum_i^{occ}|\varphi_i(\vec{r})|^2$.

This potential can be defined as the sum of the external potential, which is the Coulomb attraction between the bare nucleus and the electrons, the Hartree term, representing the electrostatic energy of the electron in the field generated by the total density; and the exchange and correlation potential (xc), thus

$$v_{\text{KS}}[n(\vec{r})]=v_{\text{ext}}(\vec{r})+v_{\text{Hartree}}[n(\vec{r})]+v_{\text{xc}}[n(\vec{r})]. \quad (7)$$

The last term of eq. 7 is the exchange-correlation potential, that takes into account the many-body effects in the form of an exchange-correlation functional and is defined by the functional derivative of the xc energy

$$v_{\text{xc}}[n(\vec{r})]=\frac{\delta E_{\text{xc}}}{\delta n(\vec{r})}. \quad (8)$$

The only approximation in DFT is related to the non-trivial many-body effects, which can be grouped into one of the terms of the non-interacting Kohn-Sham potential - the exchange-correlation (xc) functional. This functional has to be obtained by approximations, developed for a wide variety of physical systems and applications.

The simplest approximation to represent an exchange-correlation potential is to apply the Local Density Approximation (LDA) or its spin-relaxed version, the Local Spin-Density Approximation (LSDA). Within this approximation the potential depends only on the value of the density at $\vec{r}$ [22]. The correlation functional is obtained by a simple parametrized form fitted to several densities calculated by using quantum Monte Carlo simulations of Ceperley and Alder [23] on homogeneous electron gases. The most common parametrizations in use are PZ81 [24], PW92 [25].

The generalized gradient approximation (GGA), another well known functional, differs from the LDA because this functional also incorporates the effects of inhomogeneities by including the gradient of the electron density, ∇n (semi-local method). In this case the most widely used parametrizations are the Perdew-Wang (PW91) [26] and the Perdew-Burke-Ernzerhof (PBE) [27].

Some results, obtained within the L(S)DA approximation are found to be in very good agreement with experimental data, such as equilibrium structures, harmonic stretch frequencies, and charge moments [28]. Although successful for some systems, this approach can fail, for example, by incorrectly predicting negative ions to be unstable, underestimating the fundamental energy gaps of semiconductors and insulators, overestimating the length of hydrogen bonds. Similar to the LDA, GGA also fails to describe energy band-gaps, which are a crucial physical quantity if one intends to study, e.g. the impurity levels in doped semiconductors. Another common deficiency of (semi-)local approximations is their incorrect description of long-range correlation, mainly the van-der-Waals (vdW) interactions. Inspite these failures, these functionals provide reasonable accuracy for forces, charge-densities, energy barriers, and are computationally inexpensive to obtain the ground-state properties of periodic systems.

Improved exchange-correlation functionals have been formulated since then, and are grouped into five *rungs* in a sequence of chemical accuracy, known as *the Jacob's ladder of density functional approximations* [29]. As the ladder is ascended, the functionals incorporate higher levels of theory with increasingly complex parameters.

In order to obtain a *ab-initio* band-structure of bi-layer graphene, as a function of different applied electric-bias, and compare to the tight-binding approximation, DFT calculations were performed, as implemented in the Quantum-Espresso code package [30]. The semi-local generalized-gradient approximation functional with the PBE parametrization [27] was employed for electronic-structure the calculations. Projector augmented-wave (PAW) [33, 32, 31] pseudopotentials were used to represent the effective-potential of the system.

The starting point for the present calculations, was a full structural relaxation for the unit-cell of the AB stacking of bi-layer graphene, performed with a plane-wave cut-off of 900 eV. Such a high cut-off was found necessary to converge the total energy of the system. In order to sample the Brillouin zone (BZ) a Γ-centred Monkhorst-Pack mesh [34] of $44\times44\times1$ was employed. Since (semi-)local DFT functionals do not take into account van der Waals interactions, which are essential for many covalent bonded systems and systems dominated by dispersion forces, i.e. interlayer bonding of bi-layer graphene, dispersion effects were included via semiempirical atom pairwise interactions using the DFT-D2 methods by Grimme *et al* [35].

In Fig. 1 the electronic band structure is represented for the system, where one may observe that at 0 eV, the valence-band maximum and conduction-band minimum are joint together, thus exhibiting a zero band-gap at the

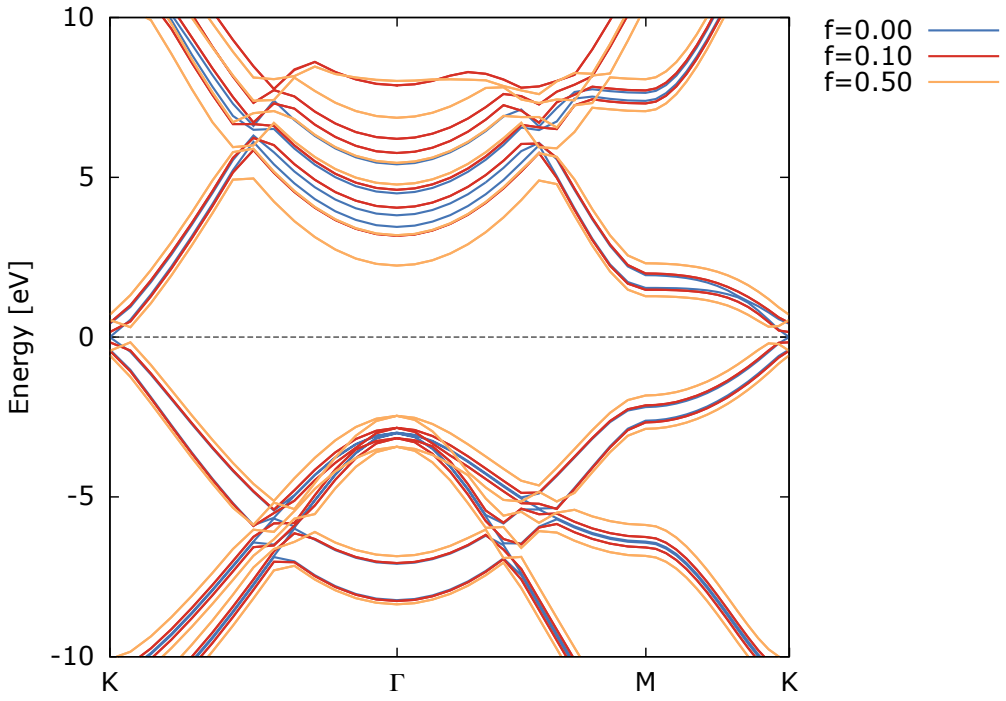

Figure 1: Electronic band-structure of bi-layer graphene for the AB-stacking system, for different applied electric-bias. The units of the electric-bias is given by eV/A.

high-symmetry point K. By applying an electric-bias, the gap starts to open. The width of the gap increases with increasing bias, evidencing a tunable electronic band-gap, similar to what was experimentally observed [36], and similar to results obtained through the tight-binding method.

References

[1] Y. Araki. Chiral Symmetry Restoration in Monolayer Graphene Induced by Kekule Distortion. *Phys. Rev. B*, 84:113402, 2011.

[2] Y. Araki and T. Hatsuda. Chiral Gap and Collective excitations in Monolayer Graphene from Strong Coupling Expansion of Lattice Gauge Theory. *Phys. Rev. B*, 82:121403(R), 2010.

[3] C. Berger, Z. Song, T. Li, X. Li, A. Y. Ogbazghi, R. Feng, Z. Dai, A. N. Marchenkov, E. H. Conrad, P. N. First, and W. A. de Heer. Ultrathin Epitaxial Graphite: 2D Electron Gas Properties and a Route Toward Graphene-Based Nanoelectronics. *J. Phys. Chem.*, 108:19912, 2004.

[4] C. G. Van de Walle and J. Neugebauer. Universal Alignment of Hydrogen Levels in Semiconductors, Insulators and Solutions. *Nature (London)*, 423:626, 2003.

[5] E. V. Gorbar, V. P. Gusynin, V. A. Miransky, and I. A. Shovkovy. Magnetic Field Driven Metal-Insulator Phase Transition in Planar Systems. *Phys. Rev. B*, 66:045108, 2002.

[6] V. P. Gusynin, V. A. Miransky, and I. A. Shovkovy. Catalysis of Dynamical Flavor Symmetry Breaking by a Magnetic Field in 2 + 1 Dimensions. *Phys. Rev. Lett.*, 73:3499, 1994.

[7] V. P. Gusynin and S. G. Sharapov. Unconventional Integer Quantum Hall Effect in Graphene. *Phys. Rev. Lett.*, 95:146801, 2005.

[8] D. V. Khveschenko, A. G. Yashenkin, and I. V. Gornyj. Interacting Random Dirac Fermions in Superconducting Cuprates. *Phys. Rev. Lett.*, 86:4668, 2001.

[9] D. V. Khveshchenko. Ghost Excitonic Insulator Transition in Layered Graphite. *Phys. Rev. Lett.*, 87:246802, 2001.

[10] D. V. Khveshchenko. Magnetic-Field-Induced Insulating Behavior in Highly Oriented Pyrolitic Graphite. *Phys. Rev. Lett.*, 87:206401, 2001.

[11] D. V. Khveshchenko. Electron Localization Properties in Graphene. *Phys. Rev. Lett.*, 97:036802, 2006.

[12] Y. Kopelevich, P. Esquinazi, J. H. S. Torres, and S. Moehlecke. *J. Low Temp. Phys.*, 119:691, 2000.

[13] K. S. Novoselov, A. K. Geim, S. V. Morozov, D. Jaing, M. I. Katsnelson, I. V. Grigorieva, S. V. Dubonos, and A. A. Firsov. Two-Dimensional Gas of Massless Dirac Fermions in Graphene. *Nature*, 438:197, 2005.

[14] K. S. Novoselov, A. K. Geim, S. V. Morozov, D. Jaing, Y. Zhang, S. V. Dubonos, I. V. Grigorieva, and A. A. Firsov. Electric Field Effect in Atomically Thin Carbon Films. *Science*, 306:666, 2004.

[15] K. S. Novoselov, E. McCann, S. V. Morozov, V. I. Fal'ko, M. I. Katsnelson, U. Zeitler, D. Jiang, F. Schedin, and A. K. Geim. Unconventional Quantum Hall Effect and Berry's Phase of 2π in Bilayer Graphene. *Nature Physics*, 2:177, 2006.

[16] N. M. R. Peres, F. Guinea, and A. H. Castro Neto. Electronic Properties of Two-Dimensional Carbon. *Annals of Physics*, 321:1559, 2006.

[17] J. Robertson. High Dielectric Constant Gate Oxides for Metal Oxide Si Transistors. *Rep. Prog. Phys.*, 69:332, 2006.

[18] G. Semenoff. Condensed-Matter Simulation of a Three-Dimensional Anomaly. *Phys. Rev. Lett.*, 53:2449, 1984.

[19] P. R. Wallace. The Band Theory of Graphite. *Phys. Rev.*, 77:622, 1947.

[20] Y.-Y. Zhang, C. Fang, X. Zhou, K. Seo, W.-F. Tsai, B. A. Bernevig, and J. Hu. Quasiparticle Scattering Interference in Superconducting Iron Pnictides. *Phys. Rev. B*, 80:094528, 2009.

[21] W. Kohn and L. Sham, Phys. Rev. 140, A1133, 1965. P. Hohenberg and W. Kohn, Phys. Rev. 136, B864, 1964.

[22] F. Nogueira, A. Castro, and M. A. L. Marques. A Primer in Density Functional Theory, chapter 6, pages 218. Springer, 2002.

[23] D. M. Ceperley and B. J. Alder, Phys. Rev. Lett. 45, 566, 1980.

[24] J. P. Perdew and A. Zunger, Phys. Rev. B 23, 5048, 1981.

[25] J. P. Perdew and Y. Wang, Phys. Rev. B 45, 13244, 1992.

[26] J. P. Perdew, J. A. Chevary, S. H. Vosko, K. A. Jackson, M. R. Pederson, D. J. Singh, and C. Fiolhais, Phys. Rev. B 46, 6671, 1992. J. P. Perdew, J. A. Chevary, S. H. Vosko, K. A. Jackson, M. R. Pederson, D. J. Singh, and C. Fiolhais, Phys. Rev. B 48, 4978E, 1993.

[27] J. P. Perdew, K. Burke, and M. Ernzerhof, Phys.l Rev. Lett. 77, 3865, 1996. J. P. Perdew, K. Burke, and M. Ernzerhof, Phys. Rev. Lett. 78, 1396(E), 1997.

[28] W. Koch and M. C. Holthausen. A Chemist's Guide to Density Functional Theory. Wiley-VCH Verlag GmbH, second edition edition, 2001.

[29] J. P. Perdew and S. Kurth. A Primer in Density Functional Theory, chapter 1, page 1. Springer, 2002.

[30] P. Giannozzi, S. Baroni N. Bonini, M. Calandra, R. Car, C. Cavazzoni, D. Ceresoli, Guido. L. Chiarotti, M. Cococcioni, I. Dabo, A. Dal Corso, S. de Gironcoli, S. Fabris, G. Fratesi, R. Gebauer, U. Gerstmann, C. Gougoussis, A. Kokalj, M. Lazzeri, L. Martin-Samos, N. Marzari, F. Mauri, R. Mazzarello, S. Paolini, A. Pasquarello, L. Paulatto, C. Sbraccia, S. Scandolo, G. Sclauzero, A. P. Seitsonen, A. Smogunov, P. Umari and R. M. Wentzcovitch, J.Phys.:Condens.Matter 21, 395502, 2009.

[31] P. E. Blöchl. Projector Augmented-Wave Method. Phys. Rev. B, 50:17953, 1994.

[32] G. Kresse and D. Joubert, Phys. Rev. B 59, 1758, 1999.

[33] $\mathrm{C.pbe-n-kjpaw\_psl.0.1.UPF}$ pseudopotential was downloaded from http://www.quantum-espresso.org.

[34] H. J. Monkhorst and J. D. Pack. Special points for brillouin-zone integrations. Phyiscal Review B, 13:5188, 1976.

[35] S. Grimme, J. Comp. Chem. 27, 1787 (2006).

[36] Y. Zhang, T.-T. Tang, C. Girit, Z. Hao, M. C. Martin, A. Zettl, M. F. Crommie, Y. R. Shen and F. Wang, Nature 459, 820, 2009.

Finite Orbit decomposition of endomaps

by N. MARTINS-FERREIRA AND M. GASPAR

Centre for Rapid and Sustainable Product Development,
Polytechnic Institute of Leiria, Marinha Grande, Portugal

Abstract: In this work we present a vectorized Matlab algorithm for the decomposition of an endomap into its finite orbits.

Keywords:

1 Introduction

Every endomap $f\colon X \to X$ induces a partition of X into disjoint orbits. Such decomposition is in general not unique. However, in this text we provide a vectorized Matlab implementation for an algorithm which can be considered as a canonical decomposition of the domain of an endomap into its finite (disjoint) orbits.

To do that we have to consider three different kind of (finite) orbits that we will call initial orbits, linking orbits and cyclic orbits.

The following definitions are useful in establishing the three different kind of orbits.

Definition Let $f\colon X \to X$ be an endomap. An element $x \in X$ is said to be:

1. a *initial point* if $card(f^{-1}(x)) = 0$;
2. a *merging point* if $card(f^{-1}(x)) > 1$;
3. a *linking point* if $card(f^{-1}(x)) = 1$.

Here $card$ stands for cardinality and $f^{-1}(x)$ is the set of all elements $x' \in X$ with $f(x') = x$.

For the purposes of this note a sequence of $f\colon X \to X$ is any subset $S \subseteq X$ together with a distinguished element $x_1 \in S$ and a map

$$\eta\colon S \to \mathbb{N}$$

such that

$$\eta(x_1) = 1$$

and for any other $x \in S$, different from x_1, there exists a unique $x' \in S$ with

$$x = f(x') \quad \text{and} \quad \eta(x) = \eta(x') + 1.$$

Each sequence (S, x_1, η) can be ordered as

$$x_1, x_2, \ldots, x_n, \ldots$$

with $x_{i+1} = f(x_i)$. The element x_1 is called the starting element and, in case S is finite, say of length n, then x_n is called the last element in the sequence.

We are now in position to define the three different kind of orbits which will be considered in this note.

Initial Orbits An initial orbit for an endomap $f\colon X \to X$ is a finite sequence (S, x_1, η) where x_1 is a initial point and $f(x_n)$, the image by f of the last element in the sequence, is a merging point. All the other points are required to be linking points.

Linking orbits A linking orbit of $f\colon X \to X$ is a finite sequence of f, say (S, x_1, η), such that both the initial point and the image by f of the last point are merging points and all the others are linking points. Observe that the image by f of the last point is no longer an element in the sequence.

Cyclic orbits A cyclic orbit of f, is any finite sequence (S, x_1, η), in which every element is a linking point and moreover $x_1 = f(x_n)$, with x_n the last point in the sequence.

Infinite orbits In this study, for practical reasons, we are excluding the infinite orbits: the ones where x_1 is an initial point and all the other are linking points.

2 Partitioning a finite domain of an endomap in its disjoint orbits

When X is not finite there is no guarantee that an endomap $f\colon X \to X$ can induce a partition on it into classes of disjoint initial, linking and cyclic orbits. However, if X is a finite set then we always have such a partition.

Proposition Let $f\colon X \to X$ be an endomap. The initial, linking and cyclic orbits of f are all disjoint. Moreover, when X is finite, they induce a partition of X.

The remaining part of this text is devoted to a vectorized (see also [1]) Matlab implementation of an algorithm to decompose a finite set X into the disjoint orbits of an endomap.

2.1 The initial and linking orbits

For practical reasons we assume that

$$X = \{1, \ldots, n\}$$

is the set of natural numbers between 1 and n and hence an endomap of X is just a vector with length n whose all entries are numbers in the range `1:n`.

The following example will be used for the purpose of illustrating the concepts:

```
f = [6, 7, 10, 2, 4, 12, 12, 13, 10, 8,  10,
    13, 13, 15, 16, 14]
```

The notion of orbit, or sequence in the sense defined above, is best illustrated by picturing the endomap $f\colon X \to X$ as a directed graph

$$X \underset{f}{\overset{1_X}{\rightrightarrows}} X$$

whose vertices are the elements of X, the edges are also the elements of X which are interpreted as follows: an element $x \in X$ is considered as an arrow (or edge)

$$x \xrightarrow{\ x\ } f(x)$$

whose domain (or source) is x and whose codomain (or target) is $f(x)$.

Our example can so be pictured as a graph in the following manner:

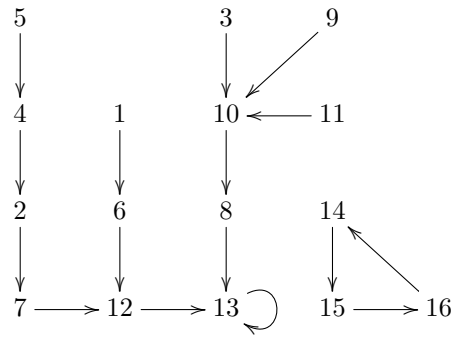

As we see it is now a simple task to visually identify the initial points:

$$1, 3, 5, 9, 11,$$

and the merging points:

$$10, 12, 13.$$

All the others are linking points.

The initial orbits are the ones which start with an initial point and run over until a merging point is found in the sequence (stopping immediately before the merging point is reached):

```
1, 6
3
5, 4, 2, 7
9
11
```

The linking orbits are the ones which start with a merging point and run over until a merging point is found in the sequence (stopping immediately before the merging point is reached):

```
10, 8
12
13
```

The remaining elements, that are not being used in any of the initial or linking orbits are organized into cyclic orbits. This is a general fact and may be stated as follows, where I is the set of all inital points, M is the set of all merging points, $IM = I \cup M$ and O_x is the set of elements in the orbit whose first element is x.

Proposition Let $f\colon X \to X$ be an endomap. If

$$Y = \bigcup_{x \in IM} O_x$$

then the restriction of f to the set $Z = X \setminus Y$ is a well defined endomap

$$f\colon Z \to Z$$

and moreover it is a bijection.

The Matlab vectorized code to obtain the initial and merging points is the following:

```
% Input: t
t=t(:); % force t to be a column vector
% check if t represents an endomap
try
    t(t);
catch ME
    error(ME.message)
end
nA=length(t);
% computing the initial points
I=setdiff(1:nA,t);
% computing the merging points
ts=sort(t);
dst=diff(ts);
M=ts(dst==0);
```

3 The cyclic orbits and its vectorized implementation

Once all the initial and linking orbits are obtained, the previous result tells us that the elements in X that where not used in the initial or linking orbits are organized into cyclic orbits. The following Matlab code is a vectorized implementation of the simple procedure of decomposing a permutation into its disjoint cycles.

```
function Orb=orbits(p)
% input: a vector p which is a
% permutation on the set A={1,...,nA};
% Output: Orb, a matrix with the
% orbits of p, one orbit in each line,
% without repeating the cycles

nA=length(p);
% force p to be a column vector
p=reshape(p,nA,1);

% Check that it is a permutation
idA=(1:nA)';
invp(p)=idA;
if ~isequal(p(invp),idA)
    disp('The input must be a permutation!')
    Orb=[];
    return
end

% the vector A will be equal to p^x,
% on each iteration x
A=p(idA);
x=1;
```

The following block of code can be improved by replacing `nA-1` by `nA/2` with the due adjustments on the rest of the code; the point is that if we arrive to the iteration `x=nA/2` then, from that moment on, there is only one cycle.

```
Z=[idA, zeros(nA,nA-1)];

L=(A~=Z(:,1));
while any(L)
    Z(L,x+1)=A(L);
    % current iteration
    A=p^{};
    A(L)=p(A(L));
    x=x+1;
    % L0 is the previous L to be
    % compared with the current one
    L0=L;
    L(L)=(A(L)~=Z(L,1));
    if ~isequal(L,L0)
        R=reduce(Z(:,1:x),L0);
        Z(R,:)=0;
        A(R)=0;
        L(R)=0;
    end
end

Orb=Z(Z(:,1)~=0,1:x);
```

The auxiliary function `reduce` is described below.

```
function R=reduce(Z,L)
% auxiliar function:
% Z and L are as above;
% R indicates the elements to be
% removed from the begining of a
% cycle because they are already
% being used in another cycles

% elements to be removed,
% initialized as false
R=false(size(Z(:,1)));

while any(L)
    Rfi=find(L,1,'first');
    % all the elements in a cycle,
    % except the starting one are
    % removed, so that they do not
    % start new cycles
    R(Z(Rfi,2:end))=true;
    L(Z(Rfi,1:end))=false;
end
```

The procedure for computing the initial and linking orbits is similar with the only difference that instead of checking whether the current iteration is equal to the starting one, one has to check if it is any one of the merging points.

An example of a (non-vectorized) implementation for computing the initial and linking orbits may be obtained as follows.

```
% I and M are computed as above
% initial merging points to be used
Orb=[]; IM=[];
labels=[]; currlab=1; % current label
for u=I
    while ~ismember(u,IM)
        Orb(end+1)=u;
        if ismember(u,M)
            currlab=currlab+1;
            IM(end+1)=u;
        end
        labels(end+1)=currlab;
        u=t(u);
    end
    currlab=currlab+1;
end
```

At this point we have computed all the initial and linking orbits, what remains is organized in cyclic orbits and hence we can use the function `perm2orb` which transforms a permutation into its disjoint orbits (see [2]).

```
% From here on we use the perm2orb
x=setdiff(t,Orb);
% find p such that t(x)=x(p) using digraph
[~,p]=digraph(x(:),t(x));
% get the orbits of p
orb=orbits(p);
% label the orbits of p
orb=orb';
[sorb1,sorb2]=size(orb);
nz=orb~=0;
orblabels=repmat(1:sorb2,sorb1,1);
orblabels=orblabels(nz);
v=x(orb(nz));

%output
s=[Orb(:); v(:)];
labels=[labels(:); orblabels(:)];
```

One last issue has to be solved for a complete implementation. We have to be able to transform the restriction of the original endomap from its original domain into the set of linking points which do not belong to any initial or linking orbit. This is done with the simple procedure of transforming any directed graph with any set of edges into a set of indexed labels, as follows.

```
function [d,c]=digraph(dom,cod)
% [d,c]=digraph(dom,cod)
% creates linear indexes d and c for dom
% and cod if dom and cod are matrices

if size(dom)~=size(cod)
    error('dom and cod must be of same size')
```

```
8  end

10 nA=size(dom,1);

12 [~,~,dc3]=unique([dom;cod],'rows');
13 % indexing the dom and cod as a linear
14 % vector of unique entries where the
15 % first nA are from dom while the last
16 % ones (nA+1:2*nA) are from cod
17 d=dc3(1:nA);
18 c=dc3(nA+(1:nA));
```

Finally we may present the output of the example considered before, which is:

Orb	Label
1	1
6	1
12	2
13	3
3	4
10	5
8	5
5	6
4	6
2	6
7	6
9	7
11	8
14	9
15	9
16	9

4 Applications Examples

Every directed graph induces an endomap. For example, the endomap f introduced in section 2.1, is derived from the graph depicted in the following diagram:

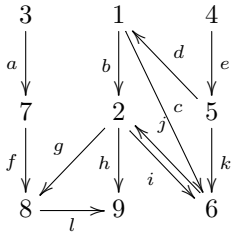

The procedure to do so is very simple: for each vertex, the incoming and outgoing edges are listed and matched. Whenever the number of incoming edges is less than the matching outgoing ones, an identity arrow is inserted. This is the case for the vertex 9, which has two incoming edges and no outgoing ones. Correspondingly, in f a loop is present (labeled as 13).

If $f\colon A \to A$ is a given endomap, then every map $g\colon A \to \mathbb{C}$, from the domain of the given endomap into the complex plane, induces a planar curve which is a realization of the graph depicting the endomap.

References

[1] M. Gaspar and N. Martins-Ferreira, *The Matlab vectorization paradigm*, CSEI, 2012.

[2] M. Gaspar and N. Martins-Ferreira, *Curves and Permutations, GTLab Technical Report*, 2012.

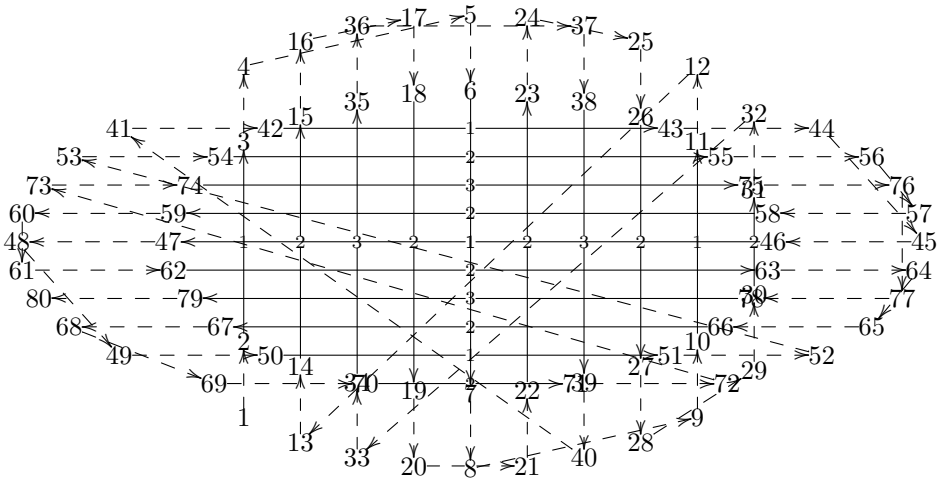

Toolpath trajectory for a multi-material extrusion of a cylindrical scaffold with orthogonal orientation from layer to layer.

The Matlab Vectorization Paradigm

by M. BELBUT GASPAR AND N. MARTINS-FERREIRA

Centre for Rapid and Sustainable Product Development,
Polytechnic Institute of Leiria, Marinha Grande, Portugal

Abstract: We give two examples of application of a vectorized programming paradigm: binary addition and cycle decomposition of directed graphs.

Keywords: Binary addition, Matlab vectorized paradigm, directed graph, cycles decomposition.

1 Introduction

This text was first presented at [5]. In this work we give two examples of application of the "Matlab way of thinking" in programming, using a vectorized paradigm [1, 3].

> A computation is vectorized by taking advantage of vector operations. A variety of programming situations can be vectorized, and often improving speed to 10 times faster or even better. Vectorization is one of the most general and effective techniques for writing fast M-code.
>
> Getreuer, in [1]

The first example is used only for educational purposes and serves as elementary example. It consists in adding one bit to the binary expansion of a number with an arbitrary length. Indeed this is a problem because the operation $(1 + 2^n) - 2^n$ returns the unexpected value of zero if n is greater than 52. The second example is concerned with directed graphs [2] and can be used to extract a simple component from a given closed path, assuming that all the self-intersections are simple.

2 Binary addition

In Matlab, the operation $(1 + 2^n) - 2^n$ returns the unexpected value of zero if n is greater than 52. This is because the system uses 64 bits to represent a number, with one bit for the signal, 52 bits for the mantissa, one bit for the signal of the exponent and 10 more bits to represent its value. This means that the number $2^{53} - 1$ is represented as a binary word with 52 ones and to add one more we would need 53 bits. This problem can be solved in several ways, for instance the fixed-point toolbox is a good option. In any case it is perhaps interesting and educational to try to solve it directly, and for that we would consider the binary representation of an arbitrary number as a vector in Matlab, with an arbitrary length, consisting only of zeros and ones. Then, in order to add one bit to it we would perform the well known procedure for binary addition of a single bit, as illustrated in the following example.

```
for i=1:length(b)
    if b(i)==0
        b(i)=1;
        break
    else
        b(i)=0;
    end
end
```

A more efficient way of doing it is to use built-in Matlab functions and vector indexing. The alternative solution is more cumbersome and difficult to decipher, but gives an example of vectorized programming in Matlab, another such example is presented in the next section.

In the first line we perform the cumulative sum of the negation of b; the result cs is the running count of the number of zeros found from the least-significant bit up to the current bit position. The expression $cs == 1$ thus gives a boolean vector with ones only between the first and second zeroes in b. The second line then sets the bits of first zero in b and up to the next zero, to one. In third line, we address the bits preceding the first zero, setting them to zero (since they originally were, by definition, ones).

```
cs=cumsum(~b);
b=b|(cs==1);
b=b&(cs~=0);
```

The performance of this implementation is in the same order of the simple decimal addition, but much faster if we take into account the need to convert from binary to decimal and back, and is limited only by the maximum length of the vector b.

3 Directed graphs and cycle decomposition

A directed graph consist of a set of vertices, a set of arrows, and two mappings; source and target, associating respectively a source and a target vertex to each arrow. The following procedure extracts a simple component from a given closed path, assuming that all the self intersections are simple. By a path with simple self intersections we mean a path where every two cycles intersect at most in one vertex, as illustrated in Figure 1(a) on next page.

Moreover, the procedure outlined is capable to determine if the output is valid or not – in other words it tell us if the given closed path is such that all self intersections are simple. An example of a path where not all self intersections are simple is shown in Figure 1(b). This process has several applications in general, in the theory of directed graphs, where the in-degree of each vertex coincides with the respective out-degree. In particular, the application where we use it is related to the slicing and scanning of triangulated surfaces in the aim of rapid prototyping manufacturing.

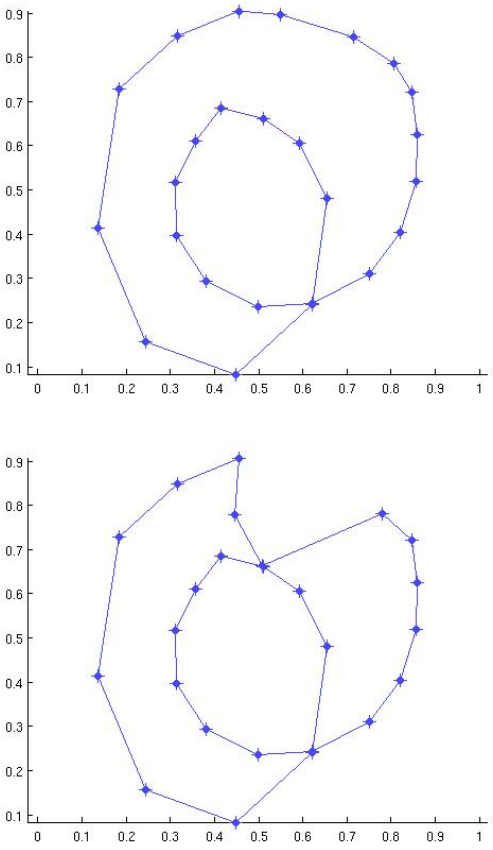

(Figure 1 - A closed path with: (a) simple self intersections; (b) non simple self intersections.)

4 The code

Given an arbitrary path P in an arbitrary directed graph (i.e. P is any vector in Matlab) the procedure returns a path with the same end points with no repetition of vertices. Example, the code described below, for P=[1 2 3 4 2 5 6 7 6 8] returns [1 2 5 6 8].

```
% idxS is such that P(idxS)=S and S is sorted
[S, idxS]=sort(P)

% idxR is such that idxS(idxR)=1:end
[~,idxR]=sort(idxS)

% mark repeated vertices in P
rep=~diff(S([1:end,1]));
n1=-diff(~rep([end,1:end]));
n=cumsum(n1(idxR));

%returns the simple path
P=P(n==0);
```

A simple change in the code above allow us to obtain the simple components of the given path.

Vectorizing your code is worthwhile for several reasons:

Appearance: Vectorized mathematical code appears more like the mathematical expressions found in textbooks, making the code easier to understand.

Less Error Prone: Without loops, vectorized code is often shorter. Fewer lines of code mean fewer opportunities to introduce programming errors.

Performance: Vectorized code often runs much faster than the corresponding code containing loops.

The reader can find a more detailed exposition on this type of programming in the references below.

References

[1] P. Getreuer, Writing fast Matlab code, 2008, http://www.mathworks.com/matlabcentral/fileexchange/5685

[2] J.M.S. Simões Pereira, Matemática Discreta: Grafos, Redes, Aplicações, Editora Luz da Vida, 2009.

[3] S. Attaway, Matlab - a Practical Introduction to Programming and Problem Solving, 2nd Edition, Elsevier, Oxford 2012.

[4] D. J. Higham and N. J. Higham, Matlab Guide, SCIAM, Philadelphia 2000.

[5] M. Gaspar and N. Martins-Ferreira, The Matlab Vectorization Paradigm, CSEI2012 – Conferência Nacional sobre Computação Simbólica no Ensino e na Investigação, Lisboa, 2-3 Abril de 2012.